Collision-induced dissociation of Fe_n^+ ($n=2$–10) with Xe: Ionic and neutral iron binding energies

S. K. Loh[a] and David A. Hales
Department of Chemistry, University of California, Berkeley, California 94720
Li Lian and P. B. Armentrout[b]
Department of Chemistry, University of Utah, Salt Lake City, Utah 84112

(Received 18 October 1988; accepted 19 January 1989)

Cross sections for collision-induced dissociation (CID) of Fe_n^+ with Xe, $2 \leqslant n \leqslant 10$, are presented. Experiments were performed on a newly constructed guided ion beam mass spectrometer, the design and capabilities of which are described in detail. The single mechanism for dissociation of iron cluster ions is sequential loss of iron atoms with increasing collision energies. There is no evidence for fission to molecular neutral products. The cross section threshold energy dependences are analyzed to give the bond dissociation energies (BDEs), $D^0(Fe_{n-1}^+-Fe)$. Data analysis employs an empirical model that incorporates RRKM theory to account for inefficient dissociation on the time scale of the experiment. Results show that Fe_6^+ has the strongest BDE, $D^0(Fe_5^+-Fe) = 3.44 \pm 0.18$ eV, while Fe_3^+ is the most weakly bound, $D^0(Fe_2^+-Fe) = 1.64 \pm 0.15$ eV. Neutral cluster BDEs are derived from ionic binding energies and known ionization potentials. Branching ratios and other cross section features are also discussed with respect to cluster size.

I. INTRODUCTION

Small transition metal clusters have aroused much interest in the past five to ten years mainly because they are novel species, but also because their study may give insight into many important processes, such as catalysis and corrosion. Recent technological advances have made gas-phase studies of these particles a reality.[1,2] Complicating solvent interactions are not present in such studies, thereby laying open elucidation of the properties of bare metal clusters. A further level of selectivity can be achieved by studying ionic clusters, as these clusters can be separated by their mass-to-charge ratios with relative ease. This property allows a single cluster to be chosen for study from an invariably complex mixture of nascent bare and often partially oxygenated clusters. Selectivity is especially useful in chemical studies, because it enables a reaction to be followed unambiguously from reactants to products. Facile control (i.e., trapping and focusing) and ease of detection are two additional advantages that ionic clusters hold over their neutral analogs.

The ability to model reactivity on a metal surface at the atomic level is a long-range goal of research on metal clusters. With a rapidly expanding data base, a rudimentary understanding seems almost within reach. Cluster studies also have the potential to provide insight into the transition between *physical* properties of the atom and those of the bulk, such as between the ionization potential (IP) and the work function.[3] Since atomic species often show much different reactivities than the bulk, similar links may also be forged between the *chemical* properties of these two regimes. The convergence of the atomic and bulk chemistries can be followed from either asymptote, but care must be taken to identify clusters or islands of cluster sizes with special properties. To date, this intermediate range of particle sizes is largely unexplored, in contrast to the relatively well characterized limits.

Many characteristics of a cluster must be elucidated for a meaningful understanding of its physical and chemical properties. There are two intertwined quantities that are especially important. One is the geometry of the cluster. The other is the strength of the bonds within the cluster. One means of obtaining this information is the use of *ab initio* theory. In particular, transition metal dimers have been modeled with *ab initio* calculations in order to obtain spectroscopic and bonding information.[4] Calculations on larger species have been scarce, though the work on transition metals clusters has recently begun.[5] The spectroscopic parameters and bonding of Fe_2 have been predicted[6] and largely experimentally verified.[7] These show that the bond largely comes from a 4*s*–4*s* interaction. Although the exact extent of 3*d* bonding is not well known, it seems that the 3*d* character is fairly small compared to the contributions from the 4*s* orbitals.[6(b),8] In larger clusters, the bonding might be expected to be similar, i.e., resulting mainly from 4*s*–4*s* interactions,[9] although a recent calculation uses substantial 3*d* contributions to model the Fe_n ($n = 2$–6) band structures.[10]

Experimentally, Fe_n has been one of the most studied transition metal clusters, due to its role in catalytic and corrosion processes. The popularity of Fe is also due to the relative ease of cluster formation and sample availability and cost. Both are such that careful and time-consuming work can be carried out, without excessive financial and experimental concerns. Previous work has produced sharp photoionization thresholds identified with adiabatic ionization potentials (IPs).[11] These, though generally decreasing from the IP of the atom, have some size-dependent structure. However, in the size range of this work, IP(Fe_n) decreases monotonically with increasing cluster size from 7.9 to 5.4 eV, except for Fe_3 which has a slightly higher IP than Fe_2.

[a] Current address: IBM, Thomas J. Watson Research Center, Yorktown Heights, NY.
[b] To whom correspondence should be addressed. NSF Presidential Young Investigator, 1984–1989; Alfred P. Sloan Fellow; Camille and Henry Dreyfus Teacher–Scholar, 1988 – 1993.

 0021-9606/89/105466-20$02.10

Extensive Fe_n hydrogenation studies ($n = 6$–29) have been performed by Richtsmeier *et al.*, in which the rates of hydrogen chemisorption were measured.[12] In combination with the flow tube measurements of Morse *et al.*,[13] the mechanism for dissociative chemisorption of H_2 on Fe_n is found to change between $n = 5$ and 6.[14] Parks *et al.*, determined the extent of Fe_n ($n \geqslant 8$) saturation with D_2O and NH_3.[15] The abrupt changes in the maximum "coverage" with size imply structural changes in Fe_n between $n = 14$–15 and also between $n = 18$–19. The Fe_{15} structure proposed is the nearly close-packed structure, bcc rhombic dodecahedron.

While reactivity studies provide one qualitative means of surmizing cluster structures or bonding schemes, another way is from "magic numbers" or species emitted from a source with high relative intensities.[16,17] From the intensity spectra, unusually stable clusters can be identified, but effects of various source conditions must be deconvoluted to unambiguously isolate true magic numbers. Magic numbers have not been observed for iron clusters to date.

Despite this intense effort to characterize transition metal clusters (and iron clusters, in particular), the bond strengths of the clusters are quantities which have gone unmeasured. It is with these as primary objectives that we undertook the set of experiments described in this work. The use of ion beam techniques has proven to be a valuable tool for providing thermochemical and kinetic insight into reactions of atomic ions with a wide variety of neutral gases.[18] In 1983, this technique was applied to Mn_2^+, representing the first determinations of a bond dissociation energy (BDE) of a bare transition metal cluster ion[19] and its chemistry.[20] Since then several prominent efforts have used this method to examine clusters including Al_n^+,[21] Si_n^+,[22] and B_n^+.[23] In this paper, these techniques are used to examine the energy dependence of collision-induced dissociation (CID) of iron cluster ions from 2 to 10 atoms. Bond dissociation energies (BDEs) of ionic and neutral clusters are derived. The dissociation mechanism is determined from branching ratios and other features in the cross sections.

II. EXPERIMENTAL

A. Overview

Experiments were performed on a recently constructed guided ion beam mass spectrometer, which heretofore has not been described in detail. An apparatus schematic is shown in Fig. 1. This instrument is designed to measure the energy dependence of reactions of cold metal cluster ions. Cluster ions are created by laser vaporization of a metal rod in a continuous high pressure flow of helium. The resulting distribution of cluster and atomic ions is focused into a 60° magnetic sector, providing a mass-selected beam of reactant ions. Interaction with a neutral gas takes place in an octopole ion guide at low pressures and at a well-defined kinetic energy. Product intensities, measured as a function of the collision energy, are then converted to reaction cross sections.

B. Cluster ion source

An earlier version of the ion source has been described.[24] Since that report, several significant modifications have been made and are discussed here. As before, clusters are created by laser vaporization of a metal sample rod followed by condensation in a high pressure He flow, a technique pioneered by Smalley[1] and Bondybey[2] and their respective co-workers. In this case, the sample is a low-carbon steel rod, 6.35 mm in diameter. The rod rotates and translates so that the tightly focused laser spot rasters across the virgin surface at a linear speed of ~4 mm/min. Sample rods have a length of 5.1 cm for sputtering, limited by the throw of

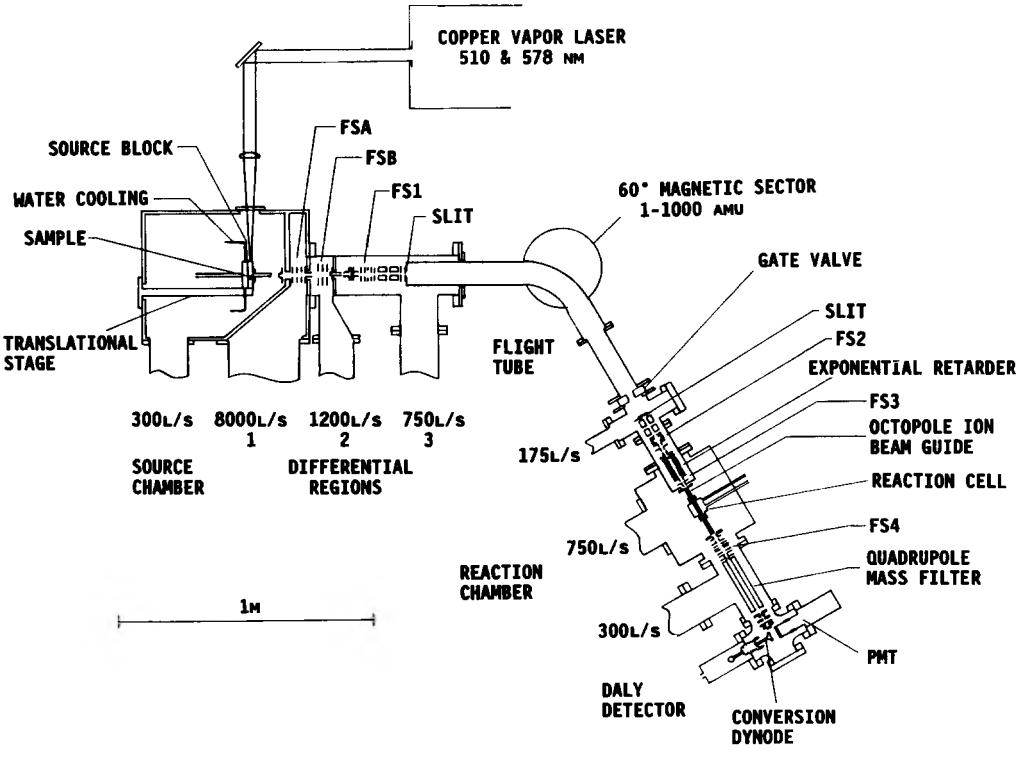

FIG. 1. Schematic diagram of the guided ion beam mas spectrometer designed to measure the energy dependences of reactions of thermalized, continuous beams of metal cluster ions. FS indicates an ion focusing stage. All pumping speeds are given for diffusion pumps, except for the source chamber which is pumped by a roots blower.

the motorized drive. Rod vaporization occurs in one slow continuous pace, without a preliminary pass often used to burn-off the outer oxide layer. The sample drive and aluminum source block are water cooled, preventing excessive heating in vacuum. Although not used in this work, a source and sample drive have been constructed to allow use of disk or foil samples.[25]

A copper vapor laser (Cooper Laser Sonics, Plasma Kinetics, CVL 351HR) was chosen as a means of metal vaporization for its high power and fast repetition rate. In these studies, the laser operates at an average power of about 24 W and a repetition rate of 7 kHz, although vaporizing powers of up to 30 W and pulse rates of 4 to 12 kHz are available. Ions are created directly in the ablation process. An ionizer is neither needed nor used. At a wavelength of 510 nm, the optimal average power for cluster ion creation is found to be between about 19 and 28 W, corresponding to pulse energies of ~3–4 mJ/pulse. Lower power creates fewer ions, whereas higher power sputters more material, occluding smooth He flow within the source in a shorter time period. Even with low laser power, partial clogging limits routine experimental time to 8 to 10 h of continuous operation, since the ion beam loses stability when directed flow is reduced. The necessary source cleaning takes about 0.5 h, so that practically continuous data collection is possible.

The high repetition rate of the laser requires a continuous flow of He. A source duty cycle of greater than 80% results, producing an essentially continuous ion beam. Helium flow is regulated and measured by a 20 000 sccm (standard cubic centimeter per second) mass-flow controller (MKS 1258B). A U-shaped liquid nitrogen trap filled with molecular sieve material removes impurities from the He, such as oxygen, which quench bare metal cluster formation. Reagents, controlled in a similar manner, can be added to the flow to create ligated metal clusters or for use as a diagnostic tool. Pulsed He flows use considerably higher helium stagnation pressures than continuous flows,[26] but the residence time of the metal vapor in the high pressure region is commensurately shorter. Within the 5.7 cm long nozzle, a typical flow of 6000 sccm of helium corresponds to ~350 Torr stagnation presure and $>10^5$ thermalizing collisions between a cluster and He. The initially narrow pulse of metal vapor is temporally broadened by turbulent mixing in the clustering nozzle.[24]

A supersonic expansion, that further cools internal modes, occurs from a 1.0 mm diam nozzle into the source region. Under these conditions, the terminal speed ratio of the expansion is calculated to be near 15, yielding a translational temperature of less than 10 K.[27] The expansion is collimated by a conical skimmer with a 2.5 mm diam orifice, located 18 nozzle diameters downstream. The source chamber is pumped by a roots blower (285 ℓ/s He) backed with a mechanical pump (59 ℓ/s) to a pressure of ~180 mTorr during operation. The source and skimmer are grounded, keeping the expansion region field-free to prevent collisions caused by ion extraction that can reheat the cluster ions. The source rests on a translational stage, permitting precise nozzle to skimmer alignment under vacuum. Behind the skimmer is a small sliding gate valve of our own design, which allows the source to be easily vented without breaking vacuum in the remainder of the apparatus.

Another major modification to the source is the addition of an extra differential pumping region (DR1). DR1 is pumped by an 8000 ℓ/s diffusion pump (Varian VHS-400) that is backed by a 25 ℓ/s mechanical pump (Sargent–Welch 1398) to typical operating pressures of 8×10^{-5} Torr. To keep the pumping speed high, a gate valve or baffle is not used. The chamber, 7.6 cm in length at the beam line, has an angled back wall to increase the effective area of the diffusion pump. DR1 allows higher He pressures within the source and a harder supersonic expansion than previously reported, yielding both better cooling and higher intensities. Cluster intensities decrease less rapidly with cluster size than observed previously. Fe^+, the most intense ion, routinely saturates our detector at $>2.5\times10^7$/s and Fe_{10}^+ has a typical intensity of 2.5×10^6/s.

Ions exit DR1 and enter a second differential pumping region (DR2). This chamber, pumped by a 1000 ℓ/s diffusion pump (unbaffled and ungated Varian VHS-4), operates near 1×10^{-6} Torr. Both DR1 and DR2 have low-voltage, three-element focusing stages (FSA and FSB) to accelerate and focus the ions. Lens elements, with 1.25 cm diam apertures, are constructed of fine mesh to maintain high pumping speeds.[28] Circular stainless steel frameworks, 3.2 cm from the beam line, align and space the lens elements. Typically focusing is necessary in DR1 for efficient ion transmission to DR2. FSA potentials of 300 V broaden the ion energy distributions perceptibly. Consequently, FSA lens potentials are kept typically at 0, − 8, and 0 V, respectively. The aperture separating the two regions (4.7 mm diam) is also kept near − 10 V. In FSB, the first element is grounded, though potentials of the other elements can exceed − 300 V and do not affect the appearance of the data.

C. Mass spectral region

After passing through DR1 and DR2, ions enter the mass spectral region via a 4.7 mm diam aperture. This region is pumped with a diffusion pump (CVC-6) and a liquid nitrogen cryotrap to operating pressures of $\sim1\times10^{-7}$ Torr. A high voltage focusing stage (FS1), similar to a low energy version elsewhere in our laboratory,[29] focuses and accelerates ions to almost 3 keV. A pair of quadrupole lenses[30] converts the ion beam from a circular cross section to a vertical ribbon shape for transmission through the entrance slit of a 60° magnetic sector. Within the circular pole faces (pole gap = 1.9 cm), ions are bent on a flight path with a radius of 26.9 cm, such that any neutrals are prevented from entering the reaction region. The momentum analyzer has 1 mm entrance and exit slits and image and object distances of 47.6 cm.[31] The mass resolution is determined to decrease with increasing mass, having measured FWHMs of 0.6 to 1.3 amu for Fe_6^+ to Fe_{10}^+. Even for the heaviest cluster studied here, Fe_{10}^+, the beam contains <0.8% of the next most abundant isotopomer. Thus, ion beams are essentially comprised of clusters of a single mass. Doubly charged ions are not emitted from the source, as demonstrated by the absence of their CID products. Apparently, in this size range, multiply

charged clusters are not formed in the high pressure source or may fragment to singly charged moieties, because of "Coulombic explosions."

Flight tube positioning within the pole faces is modified to account for fringing fields as suggested by Coggeshal and others.[32] Final positioning is empirically determined by maximizing mass resolution. The flight tube, at a potential of ~ -3 kV, is isolated from the magnet pole faces by mica sheets. An integral gate valve on the flight tube separates the interaction region from the source and differential chambers. To reduce ion scatter, a diffusion pump (Edwards Diffstak model 63), also isolated from high voltage, pumps the flight tube.

After passing through the exit slit, the mass-selected ion beam is reshaped to a circular cross section by a second pair of quadrupole lenses. Ions are focused by the FS2 lens train for transmission through a limiting aperture, 0.80 mm diam. Then an exponential retarder[33] decelerates ions from energies of 3 keV to near 40 eV. The retarder consists of 41 evenly spaced lens elements with exponentially decreasing potentials set by internal resistors. Our design uses a magnification of 6.2 and an angular divergence of 1 rad/in. The potentials of the final three plates are externally controllable, but are typically set near -40 V.

D. Interaction region

An einzel lens focuses ions emerging from the retarder to the entrance of the octopole ion beam guide, which passes through a reaction cell. Another lens ensures accurate and efficient ion injection into the ion guide. The octopole consists of eight cylindrical molybdenum rods, 0.318 cm in diam, positioned on a 1.72 cm diam circle, simulating rods of hyperbolic cross section.[34] The high conductivity of Mo minimizes octopole contact potentials and keeps the octopole at 305 K during operation. Opposing phases of high voltage rf are put on alternate rods to produce a radial potential well, which for rods of hyperbolic cross section, is described by[35]

$$U_{\text{eff}}(r) = \frac{4q^2V_0^2}{m\omega^2 r_0^2}\frac{r^6}{r_0^6}, \qquad (1)$$

where q and m are the charge and mass of the ion, r_0 is the inner radius of the octopole, r is the distance from the central axis, ω and V_0 are the rms voltage and frequency of the rf, respectively. The resulting potential well has a fairly flat bottom and steeply rising walls, enabling the octopole to be used as a radial ion trap. Ion translational energy along the axis is not perturbed, but ions with transverse energies are effectively trapped. The advantages over a quadrupole ion trap have been previously discussed.[34] The octopole can also be used as an efficient retarding energy analyzer, since ion divergence due to space charge and stray fields is virtually eliminated. In beam-gas experiments such as performed here, product ion collection is also enhanced as losses due to scattering are minimized. Other advantages of an octopole for cross section energy dependence measurements have been discussed elsewhere.[29]

Studies were performed with a frequency of 6.3 MHz as set by a signal generator (Tektronix 602). The waveform is amplified by a 100 W rf amplifier (ENI 2300) followed by a resonant LC circuit formed by a 20 μH inductor and the collective capacitance of the rods and external capacitors. As a result, alternate rods have potentials that differ by up to 1000 V rms. An impedance matching circuit allows access to a wide range of resonant frequencies to provide optimal trapping for different masses,[36] a capability not used here for products of widely varying masses. Typical rod potentials are estimated at $\sim$400 V rms, though diagnostics show that efficient trapping is achieved with as little as $\sim$100 V rms. The octopole dc bias, set by a Kepco BOP-500M power supply, represents the nominal interaction energy, since the ion source is held at ground potential. In the present configuration, interaction energies can be swept from 0 to 500 eV.

The octopole passes through a stainless steel gas cell where reaction takes place. The reaction cell has a cylindrical main section 5.1 cm diam and 5.1 cm long, with exit and entrance aperture tubes 2.0 cm in diam and 3.2 cm in length. This geometry has an effective path length of 8.26 cm as calculated using a trapezoidal pressure fall-off approximation. The calibration of the reaction cell length was verified by measuring cross sections of the well-characterized ion–molecule reactions, $Ar^+ + D_2$ [29] and $Ar^+ + O_2$.[37] The reaction region is pumped with a water-baffled diffusion pump (CVC-6). Operating pressures are about 2×10^{-6} Torr, such that the ratio of pressures inside and outside the reaction cell is maintained at 100. Reactant gases are admitted via a variable leak valve (Granville–Phillips) to pressures that are measured by a capacitance manometer (MKS 298H, 1 Torr head). Pressures are about 0.1 mTorr to severely minimize the probability of multiple collision events. Product and unattenuated reactant ions that drift to the end of the ion guide are extracted from the octopole by a lens kept at -600 V. These ions are then focused by a fourth focusing stage (FS4) into a quadrupole mass filter.

E. Post-reaction mass detection

The intensities of the products and unreacted ions are typically monitored by allowing ions of a particular mass to pass through the mass filter and on to the detector. Intensities at each mass are measured for 0.5 s, so that disparate masses are sampled consecutively with rapidity. In this mode of data collection, a quadrupole mass filter is advantageous, because it lacks the hysteresis found in magnetic sectors. With any mass spectrometer, quadrupole mass filters included, consideration must be given to mass discrimination, due to mass spectrometer characteristics or reaction dynamics. These may be a problem for widely separated masses or for relatively light CID product masses, as discussed later. Efficient ion transmission through the mass filter helps to minimize these effects. The quadrupole (Extrel 150 QC with C60 electronics) has a mass range of $\sim$1000 amu and employs large rods (1.59 cm) and a low frequency (880 kHz) to maximize ion transmission. To increase transmission further, the ELFS lens supplied with the quadrupole is not used.[38] Also, the quadrupole dc bias is held at -100 V with respect to the ion source for enhanced ion transmission, although this degrades the quadrupole mass resolution to

some extent. In this regard, product resolution is not a concern in these Fe_n^+ systems, since cluster masses are separated by ~56 amu. The lowest available quadrupole resolution is used (20 amu FWHM) in order to increase ion transmission and reduce mass discrimination.

Mass-analyzed ions are extracted from the quadrupole by a high voltage einzel lens and then detected with a Daly detector.[39] The conversion dynode, held at -28 kV, provides extra gain. Scintillator and a photomultiplier (Hamamatsu R1332) are used to detect electrons ejected from the converion dynode. The photomultiplier base is similar to that suggested for an RCA 8850 tube,[40] though it has been modified for fast rise times and high currents. The detector counts single events with a maximum count rate of 25 MHz. The Daly detector is superior to the electron multiplier previously used.[24] It is more reliable, has higher sensitivity, and eliminates rf pickup from the laser, since it is better shielded.

The detector and quadrupole regions are pumped by a diffusion pump (Edwards Diffstak model 125) chosen for high pumping speed and low backstreaming rate. The detector is pumped indirectly to reduce contamination of the conversion dynode with pump oil, which does not appear to be a problem under normal circumstances.

F. Data acquisition

Unamplified signals from the photomultiplier are fed into a 50 MHz voltage discriminator (Canberra 1428A), used in the leading edge mode. Output pulses from the discriminator then go to other NIM modules: a Tennelec TC526 linear rate meter (for visual counting) and a Canberra 2071 counter/timer. The latter sets the signal collection time per mass and integrates pulses. Data acquisition is facilitated by a DEC PDP 11/73 microcomputer via an IEEE 488 bus. An experimental scan, controlled by an interactive program, consists of setting the collision energy and then setting the quadrupole to a mass of interest. After counting for 0.5 s, the next mass is set. When the masses of the reactant and all products have been scanned, a new energy is incremented and the process repeated. Consecutive scans, in which the reactant gas is routed to the chamber rather than the gas cell, measure reactions that occur with the background chamber pressure. As a result, these serve as background scans and establish the zero signal level. Foregrounds and background scans are repeated until the noise reaches an acceptable level. Computer control of the interaction energy and the quadrupole mass are accomplished by use of two 12 bit DAC converters per task to provide enhanced resolution. Two electropneumatic valves that set reactant gas flow are controlled by digital outputs under software control. Raw data is stored on a hard disk or 8 in. floppy disks.

G. Data analysis

Measured intensities are converted to a total cross section via

$$I_r = (I_r + \Sigma I_p)\exp(-\sigma_{\rm tot} n_D l), \quad (2)$$

$$\sigma_p(E) = \sigma_{\rm tot}(I_p/\Sigma I_p) \quad (3)$$

as outlined previously for this procedure.[29] Raw background counts are subtracted from the foreground before cross sections are calculated. Subscripts r and p refer to the attenuated reactant and the pth product, n_D is the reactant gas number density, and l is the effective path length. Individual product cross sections are calculated in Eq. (3). The collision energy of an ion (with mass m) and a neutral reactant (with mass M) is converted from the lab to center-of-mass (c.m.) frames by using $E(\text{c.m.}) = E(\text{lab}) \times M/(m+M)$. The absolute uncertainty in the energy scale is ± 0.05 eV, lab frame.

The uncertainty in the absolute magnitudes of the cross sections is $\pm 30\%$, mainly due to the uncertainties associated with the gas cell length and measurement of the pressure. Relative cross section uncertainties are estimated at 5%, assuming efficient product collection. Product collection appears to be excellent for $Fe_2^+ \rightarrow Fe^+ + Fe$,[8] and for dissociation of larger cluster ions to the larger daughter ions, as will be discussed. For these cross sections 5% is probably a good estimate of the relative uncertainties. On the other hand, fragmentation of larger clusters to smaller fragment ions, such as $Fe_{10}^+ \rightarrow Fe^+$ or Fe_2^+, are more strongly affected by the dynamics of the CID process. Light product ions can be scattered at large angles, whereas heavier ions are constrained to much smaller angles, due to conservation of momentum. Ions with high transverse kinetic energies can be lost in the FS4 lens train and the quadrupole itself, leading to less efficient product detection. For the larger reactant cluster ions, the lowest mass product ions probably have uncertainties that can be as high as 50%, but are reproducible to $\pm 20\%$.

III. CID CROSS SECTION ANALYSIS

A. Dissociation thresholds

In concept, obtaining information from CID cross sections is an easy task. The threshold represents the barrier to dissociation, or the endothermicity assuming that activation barriers are not present. This assumption has generally proven to be valid for ion–molecule reactions without barriers due to spin or orbit constraints.[41] Since structures and electron configurations for the cluster ground and excited states are not known, barriers due to these considerations cannot be forecast with complete certainty; however, some simple ideas probably hold. To examine processes such as $Fe_n^+ + Xe \rightarrow Fe_{n-1}^+ + Fe + Xe$ more closely, we can envision the dissociation process in reverse, where Fe interacts with Fe_{n-1}^+. All potential surfaces are attractive at long range, due to the attractive ion-induced dipole potential. Now suppose that ground state products $Fe + Fe_{n-1}^+$, do not correlate diabatically to the ground state of Fe_n^+, but to a low-lying excited state. Instead, an excited state dissociative asymptote leads to ground state Fe_n^+. Upon approach of Fe to Fe_{n-1}^+, extensive mixing of these surfaces should occur, due to the extremely high density of low-lying electronic states that are expected to result from interactions with the weakly bonding cluster $3d$ cores.[42] This mixing results in avoided surface crossings such that, even in this scenario, the ground state products are likely to correlate adiabatically to Fe_n^+ without barriers in excess of the dissociation energy. Therefore, we assume that the threshold for dissociation

(E_0) corresponds to the endothermicity of dissociation, i.e., the primary bond dissociation energy.

If Fe_n^+ dissociates by sequential loss of Fe atoms (i.e., atomic dissociation) to form the ionic molecular fragment Fe_m^+, the threshold corresponds to the sum of the cluster binding energies given by

$$E_0(\text{atomic}) = \sum_i^{n-m} D^0(Fe_{n-i}^+\text{–Fe}). \quad (4)$$

For loss of the primary Fe atom, $Fe_n^+ \rightarrow Fe_{n-1}^+ + Fe$, Eq. (4) reduces to

$$E_0(\text{primary}) = D^0(Fe_{n-1}^+\text{–Fe}), \quad (5)$$

where the threshold is *equal* to the cluster BDE. For molecular fragmentation, the situation is somewhat more complex since some bonds in the neutral fragments remain unbroken. The threshold represents the energy required to remove atoms from the cluster [Eq. (4)] minus the BDEs of the molecular fragment(s), Fe_p. The result is shown in

$$E_0(\text{molecular}) = E_0(\text{atomic}) - \sum_i^{p-1} D^0(Fe_i\text{–Fe}). \quad (6)$$

Thus, solution of Eq. (6) is a building-up process, where the BDEs of smaller ionic and neutral fragments must be known in order to extract information on a larger cluster.

B. Effect of collision gas

In practice, determining thermochemistry from CID processes is a more trying assignment. One complicating factor, which is not well understood, is the choice of the inert collision gas. The gas used for this purpose has been found to be important in accurate threshold determinations.[43] Figure 2 shows the energy dependence of Fe_2^+ and Fe_{10}^+ CID with Xe and Ar used as collision gases. In CID of Fe_2^+ with Xe, the cross section rises quickly from threshold, reaching a constant value near 8 eV. With Ar, the cross section rises more slowly from a higher apparent threshold and peaks at higher energies, demonstrating that Ar is much less efficient at promoting dissociation. The CID cross sections of $Fe_{10}^+ + Rg \rightarrow Fe_m^+ + (10-m)Fe + Rg$, $m = 9$–7, are also shown in Fig. 2, where Rg are the rare gases Xe and Ar. The apparent energy thresholds to dissociation appear nearly identical for Ar and Xe, but dissociation is again considerably more efficient with Xe. Sensitivity is therefore more important for accurate interpretation of CID with Ar and lighter collision gases. In preliminary CID studies of Co_2^+,[44] helium is found to be almost totally ineffective at promoting dissociation.

The decrease in CID efficacy with decreasing masses is discussed in detail elsewhere and is believed due to two factors.[43] Lighter collision gases require higher lab kinetic energies to provide the same c.m. collision energies. Thus, use of gases like Ar or He shortens the ion–Rg interaction time at a given c.m. energy. The polarizability of the collision gas is another important factor. Gases with higher polarizabilities, Xe for example, should be more effective at causing dissociation.

The comparison of CID with Ar and Xe leads to the question, is CID with Xe efficient enough? It is, according to

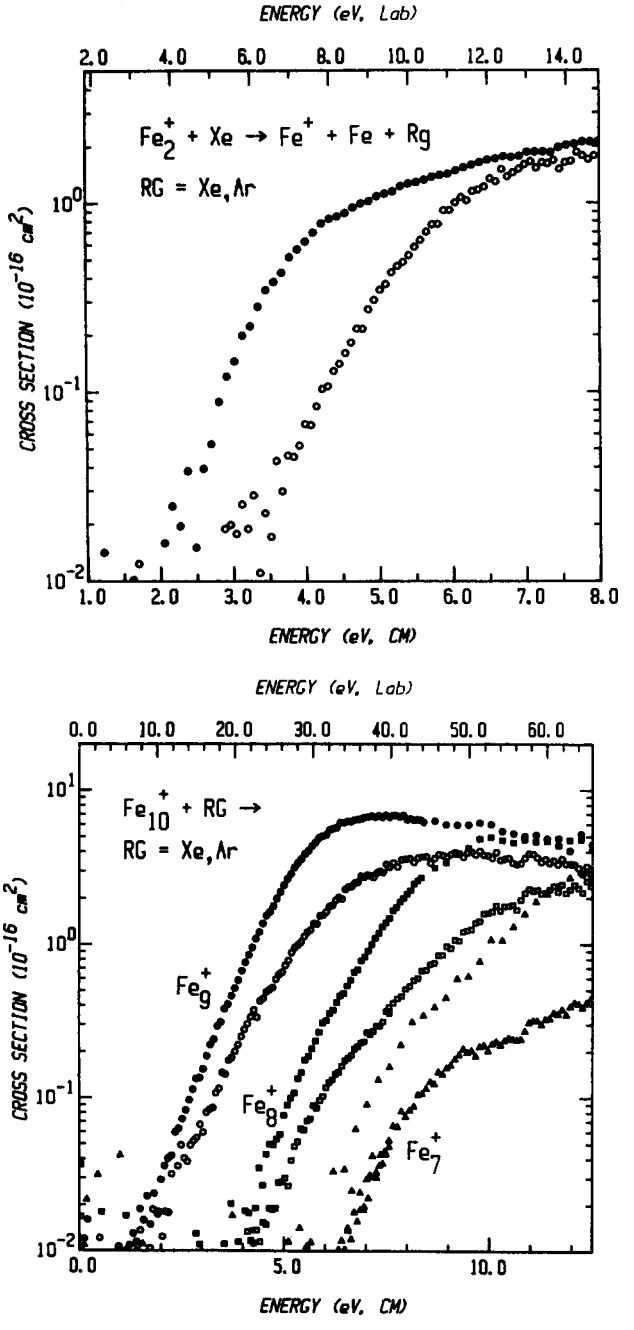

FIG. 2. Comparison of collision-induced dissociation of (a) Fe_2^+ and (b) Fe_{10}^+ with different collision gases. A much sharper threshold is observed by using Xe (solid symbols) than using Ar (open symbols) as a collision gas. Cross sections are shown as functions of collision energy in the center-of-mass (lower x axis) and, for the Xe system, laboratory (upper x axis) frames.

several past studies. CID with Xe and Kr have produced accurate thresholds for thallium halides.[45] Xe was found to give an accurate estimation of the well-known VO^+ BDE.[44] For small iron clusters, we have found that our $Fe_2^+ + Xe$ CID study yields a BDE that is in excellent agreement with photodissociation results.[46] For larger clusters, the results of Fig. 2 suggest that the CID threshold is not as sensitive to the collision gas as for smaller clusters. While additional work is warranted on this interesting effect, Xe is the heaviest, most polarizable, nonreactive gas that is conveniently handled.

Hence, in the absence of more definitive studies, we assume that Xe is an effective CID gas.

C. CID threshold modeling

With these concerns registered, closer examination of the CID process is warranted. To cause dissociation, energy must be transferred into internal modes of the cluster by a collision with Xe. When this amount of energy exceeds the dissociation threshold, the cluster can fragment. The amount of energy deposited depends on two factors: the collision energy and the efficiency of the energy transfer process. The collision energy is a distribution that depends on the thermal motion of Xe and the ion energy distribution. The distribution of the relative kinetic energy due to the thermal motion of the Xe at 1 eV have FWHMs[47] of 0.37 and 1.6 eV for Fe_2^+ and Fe_{10}^+, respectively. The ion energy ranges from about 0.27 to 0.10 eV, c.m. frame, for these two ions, respectively. These distributions can be accounted for as previously outlined.[29]

For monoenergetic collisions between Fe_n^+ and Xe, the energy imparted to the cluster depends on the reactant orientation and impact parameter. Here, the orientation of the cluster is treated as an average quantity, since cluster geometries are not known, but the effect of different impact parameters can be explicitly accounted for. Large impact parameters that result in glancing collisions, are less efficient at energy transfer than smaller impact parameters, which may have efficiencies close to unity. At threshold, a collision must have a zero impact parameter for reaction to occur. An ensemble of collisionally energized clusters has a distribution of internal energies due to the distribution of impact parameters. Clearly, with identical impact parameters and molecular orientations, more energetic collisions can transfer more energy than low energy collisions. For this reason, in the threshold region, CID cross sections should increase with increasing energies. At high collision energies, nearly all impact parameters in which collision occurs cause dissociation. As a result, an apparent hard-sphere cross section is eventually reached.

The threshold energy dependence is assumed to reflect the energy dependence of the number of quantum states available for reaction and less so dynamic effects due to intermolecular forces. The result is a statistical model that should be valid for dissociation processes of heavy particles that have large numbers of states available. These models yield a general excitation function given by

$$\sigma_p(E) = \sigma_0(E - E_0)^N/E, \tag{7}$$

where E and E_0 are the collision and threshold energies. σ_0 is a scaling factor and N is an adjustable parameter. Past work has shown Eq. (7) to be sufficiently general to describe the threshold behaviors of numerous endothermic ion–molecule reaction cross sections and provide accurate reaction thermochemistry.[48]

This model has been derived for and applied to only the simplest CID processes, atom–diatom interactions. To model the energy dependence of such systems, Maier used statistical arguments to derive Eq. (7),[49] and found N to lie between 1 and 2. On the other hand, Levine and Bernstein (LB) used an optical analysis to find a similar form, employing $N = 2.5$.[50] Then, also based on a statistical treatment, Rebick and Levine obtained $N = \sim 2$ or 1.5 for direct and indirect CID processes, respectively. Their formulation converges to that of LB with simplifying assumptions. In a series of three papers, Parks *et al.* also used optical analyses to derive Eq. (7) and applied the model to CID of thallium halides to ion pairs.[45] They found that N increased with heavier halides and collision gases.

Chesnavich and Bowers[51] have proposed a model based on transition state theory where only translational energy is considered to contribute to the reaction coordinate. This treatment provides a general form of Eq. (7) that predicts $N = 1.5$ for direct reactions of the type $Fe_n^+ \rightarrow Fe_{n-1}^+ + Fe$. We find that this form and closely related forms of Eq. (7) provide good descriptions of the cross section threshold behaviors in this work.

None of these models account for molecules with energy in excess of the dissociation energy that do not dissociate within our experimental time window. In our experiments, cluster ion dissociation must occur during flight from the gas cell to the quadrupole entrance for product observation. While this time τ changes somewhat with the kinetic energy of the ions, it is about 1×10^{-4} s (as measured by pulsing the ion beam) for the experimental conditions of interest here. Dissociation should become increasingly inefficient for larger clusters with more modes where internal energy can randomize. This effect can be estimated by RRKM theory, which predicts the unimolecular rate of dissociation of an energized molecule. It has been pointed out that the use of RRKM theory may not be directly applicable to species like metal clusters where there is a high density of vibrational and electronic states.[52,53] Finding a better model for the dissociation behavior of metal clusters is an area of active investigation, and is beyond the scope of the present work and our present instrumentation. With this proviso, we use RRKM theory to obtain at least a plausible estimate for how the time scale of dissociation might affect the observed CID threshold.

To calculate an RRKM rate constant $k(E)$, the appropriate density and number of states are required. To obtain these, we use a treatment similar to that of Jarrold and Bower,[54] in which vibrational frequencies are calculated from the Debye model of solid state physics.[55] The absolute accuracy of the frequencies are somewhat questionable, being derived from the bulk. But these frequencies may be less problematical than they appear, because some errors cancel in the division of the number of states by the density of states. Without known cluster frequencies, the Debye model presents, at worst, a good starting point. States are counted with a direct count algorithm using an RRKM program developed by Hase and Bunker.[56] The calculated RRKM rate constants for CID of Fe_n^+ (n = 4–10) are shown in Fig. 3 as a function of $E - E_0$, the internal energy in excess of the dissociation energy, for the case where $E_0 = 2.0$ eV for comparison purposes. In our model, as the cluster binding energies increase, the cluster frequencies remain the same, being derived from the invariant dimer and Debye frequencies. This is clearly one limitation of the model since the frequencies should or-

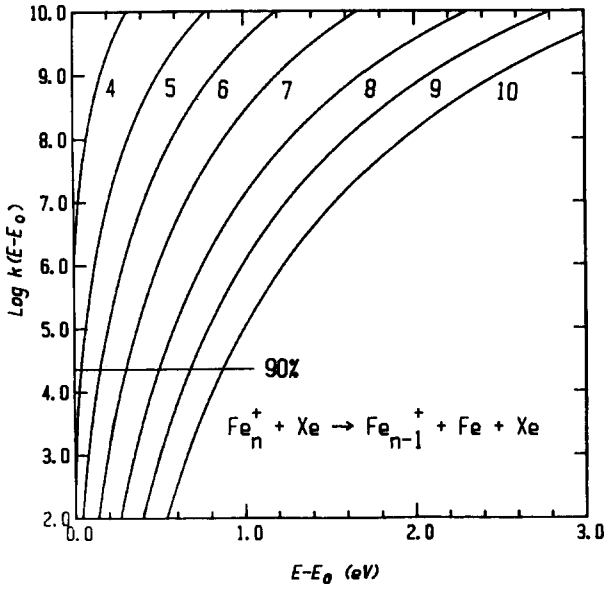

FIG. 3. Calculated RRKM unimolecular rate constants for small iron clusters, $Fe_n^+ \rightarrow Fe_{n-1}^+ + (n = 4\text{–}10)$, using frequencies derived from the Debye model. The log of $k(E - E_0)$ are plotted as functions of internal energy in excess of $E_0 = D^0(Fe_{n-1}^+\text{–}Fe)$, which is held at 2.0 eV for comparison. The line represents the 90% dissociation level on the experimental time scale for dissociation.

dinarily increase with bond strength.

Energized molecules have a distribution of internal energies, due to the distribution of impact parameters of the collisions. Therefore, a distribution of $k(E)$s and dissociation probabilities $P(E)$s are calculated. In this model, the distribution depends on the impact parameter, collision energy, and τ. τ changes with interaction energy, because the flight time in the octopole is energy dependent. This effect is negligible, however, because rate constants rise very rapidly with increasing energy. The rate necessary for 90% dissociation on our experimental time scale is shown in Fig. 3 as a dashed line.

To model the data, Eq. (7) is convoluted over the $P(E)$s derived from the RRKM rate constant. The resultant form, given in the Appendix, models the effects of different collision impact parameters on the cross section energy dependence. Dissociation of small clusters are insensitive to RRKM considerations, because the dissociation rates are sufficiently fast that dissociation is complete even at very low energies above threshold. In these cases, Eq. (A7) reduces to Eq. (7). RRKM considerations is most important for larger clusters, as indicated by the energies necessary for 90% dissociation probabilities on our experimental time scale, shown in Fig. 3. In either case, the model is convoluted over the experimental energy distributions (the ion energy spread and the thermal motion of Xe). The resulting model cross section is compared to the data and the parameters N and E_0 optimized to give the best fit by using a linear least-squares criterion.

IV. RESULTS AND DISCUSSION

A. General cross section features

Figure 4 shows the cross section energy dependences of $Fe_n^+ + Xe$, for $n = 2\text{–}10$. The dimer ion can break apart only into $Fe^+ + Fe$. With larger cluster ions, dissociation can proceed via numerous product channels, many of which are distinguished solely by the accompanying neutral fragments. For examply, $Fe_3^+ + Xe$ has two possible ionic products, but three possible product channels: $Fe_2^+ + Fe$, $Fe^+ + Fe_2$, and $Fe^+ + Fe + Fe$. By Fe_{10}^+, there are nine possible ionic products leading to 93 distinct dissociation pathways. Since we detect only ions, such pathways must be identified by thermochemical arguments or by features in the cross sections. For all clusters, Fe_{n-1}^+ production can only occur by loss of an Fe atom and thus is unambiguously identified. As will be seen in these systems, the mechanism for the formation of the other products is also quite clear.

The cross section for CID of Fe_2^+ has been discussed previously in detail.[8] It rises from a threshold of 2.72 eV to peak just above 10 eV at a magnitude of about 3 Å^2 as seen in Fig. 4. As expected for a CID process, the cross section remains relatively flat at higher energies. Since the cross section does not decline appreciably with higher energies, Fe^+ product collection appears to be efficient.

CID of Fe_3^+ forms both possible ionic products, Fe_2^+ and Fe^+. The lowest energy process, dissociation to $Fe_2^+ + Fe$, has an energy threshold of ~ 1.7 eV. $\sigma(Fe_2^+)$ rises and peaks at near 5 eV, then slowly decreases with higher energies. Observation of the Fe^+ product begins at ~ 5 eV. $\sigma(Fe^+)$ rises until ~ 9 eV, after which a slower rise with increasing energy to the highest energies is observed. As a result of the two cross section behaviors, the total cross section (i.e., the sum of the individual cross sections) is flat at higher energies. This indicates that the total ion product intensity remains nearly constant throughout this energy range and implies efficient product collection.

All three expected ionic products are observed in CID of Fe_4^+ with Xe, as shown in Fig. 4. $Fe_4^+ \rightarrow Fe_3^+ + Fe$, the primary reaction pathway, is the dominant low energy process. $\sigma(Fe_3^+)$ rises and peaks at ~ 5 eV, near the threshold for $\sigma(Fe_2^+)$. A fairly sharp decline is then noted for several eV, as $\sigma(Fe_2^+)$ rises abruptly. The decline in the Fe_3^+ cross section becomes more gradual with increasing energies. Although $Fe_3^+ + Fe$ is the most probable product channel at low energies, above 15 eV the major ionic product becomes Fe_2^+. The Fe^+ channel is at least one order of magnitude less probable than these, even at the highest energies examined here. The total cross section levels off at 5 eV, remaining constant to higher energies.

$Fe_5^+ + Xe$ yields four ionic products. Unlike CID of Fe_4^+, the dominant product of Fe_5^+ CID at all energies is loss of a single Fe atom. This process peaks at 5–6 eV then decreases slowly with higher energies. Fe_3^+ and Fe_2^+ are major product ions with higher thresholds, Fe^+ production, on the other hand, is much less probable, as evidenced by the small $\sigma(Fe^+)$ magnitude of $\leqslant 0.1$ Å^2 and the scatter in the data. The total cross section rises quickly from threshold to 5 eV, then continues to rise very slowly at higher energies.

The cross sections for $Fe_n^+ + Xe$, $n = 6\text{–}10$, show some of the same energy dependences as $n = 2\text{–}5$ and are discussed together. For the larger clusters, some lower mass products are not observed, presumably due to their small

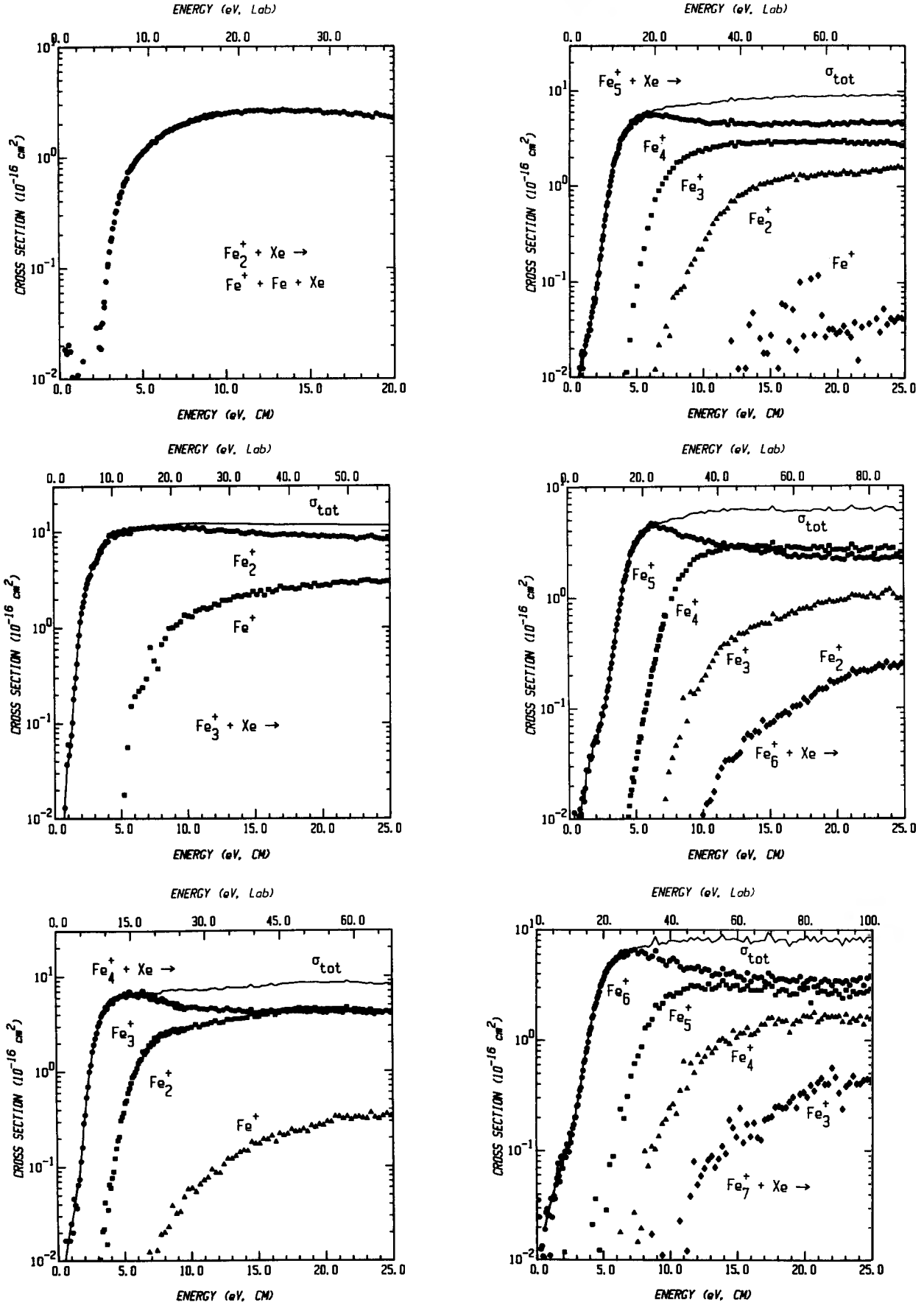

FIG. 4. Results for collision-induced dissociation of iron cluster ions, $Fe_n^+ + Xe$, $n = 2$–10 are given in parts a–i, respectively. The cross sections, measured in Å^2, are plotted as a function of collision energy in the center-of-mass (lower x axis) and laboratory (upper x axis) frames. Solid lines represent the total cross sections for dissociation.

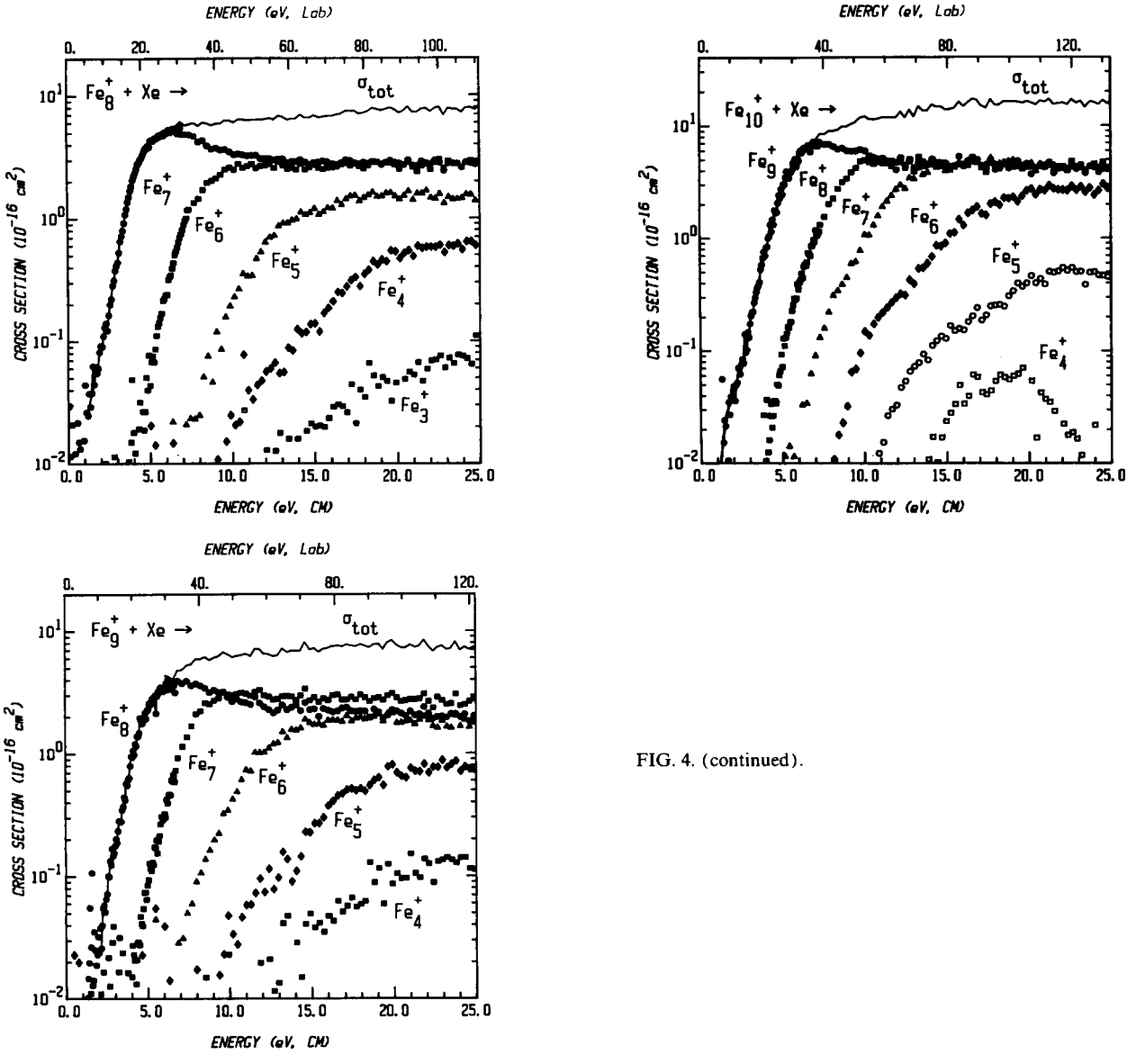

FIG. 4. (continued).

intensities and our experimental sensitivity. These ions can probably be observed at higher interaction energies, where more extensive fragmentation occurs. As discussed above, CID mechanism can influence product detection. This may be important for product channels that involve extensive fragmentation, since dissociation energy can be carried away as translational energies of the many products. As a result, inefficient fragmentation may be observed as large kinetic shifts for such processes.

The cross sections show much the same behavior as noted in CID of the smaller clusters. The lowest energy product in all cases is Fe_{n-1}^+ formed by loss of a single Fe atom. As the collision energy increases, Fe_{n-2}^+, Fe_{n-3}^+, and smaller ionic products are formed sequentially and with generally much smaller cross sections. As one product cross section peaks, formation of the next product begins. The total cross sections also have similar energy dependences to those of CID of the smaller clulsters. These rise with the Fe_{n-1}^+ product and remain fairly constant at higher energies.

The magnitudes of σ_{tot} show that Fe_2^+ has the smallest cross section, as is expected for the cluster with the smallest collision cross section. Fe_3^+ appears to have an unusually high cross section for dissociation of ~ 10 Å^2. With increasing cluster size, the total cross section then remains 7–9 Å^2 until Fe_{10}^+, where a magnitude of 15 Å^2 is observed. The high energy behavior noted for Fe_4^+, in which $\sigma(Fe_{n-2}^+)$ becomes favored over $\sigma(Fe_{n-1}^+)$ with increasing energies, is also generally observed for the larger even numbered clusters ($n = 4, 6, 8$). For the odd numbered clusters ($n = 3, 5, 7$), $\sigma(Fe_{n-1}^+)$ is larger than $\sigma(Fe_{n-2}^+)$ at all energies. Fe_9^+ diverges from this trend as Fe_7^+ is the dominant high energy product. CID of Fe_{10}^+ yields equal branching ratios at higher energies.

B. Ionic and neutral cluster binding energies

$D^0(Fe_{n-1}^+$–Fe), $n=2$–4. The lowest energy processes, $Fe_n^+ \rightarrow Fe_{n-1}^+ + Fe$, are unambiguous and free of secondary processes and product channel competition that complicates analysis. Since the rate of dissociation is high, threshold

TABLE I. Threshold analysis of Fe_n^+ CID.

n	E_0[a] (eV)	N	RRKM[b] shift (eV)	ΔE_0(I)[c] (eV)	ΔE_0(II)[d] (eV)	$D^0(Fe_{n-1}^+-Fe)$[e] (eV)
2	2.72(0.07)	1.35(0.10)	0.0	...	...	2.72(0.07)[f]
3	1.64(0.15)	1.6 (0.10)	0.0	−1.06(0.15)	2.35(1.0)	1.64(0.15)
4	1.99(0.15)	1.6 (0.10)	0.0	+0.36(0.15)	2.85(1.0)	1.99(0.15)
5	2.41(0.20)	1.5 (0.15)	0.05(0.05)	+0.44(0.15)	2.67(0.20)	2.50(0.18)
6	3.29(0.25)	1.6 (0.15)	0.10(0.07)	+0.97(0.15)	3.55(0.25)	3.44(0.18)
7	3.10(0.25)	1.5 (0.15)	0.15(0.07)	−0.09(0.15)	3.32(0.25)	3.26(0.21)
8	2.59(0.25)	1.5 (0.15)	0.23(0.10)	−0.50(0.15)	2.86(0.30)	2.74(0.23)
9	2.83(0.30)	1.7 (0.15)	0.26(0.12)	+0.37(0.15)	2.70(0.35)	2.88(0.27)
10	3.10(0.35)	1.9 (0.20)	0.45(0.15)	...	...	3.10(0.35)

[a] From analysis using Eq. (A7). Uncertainties are in parentheses.
[b] Difference in analysis with Eqs. (A7) and (7), with and without RRKM considerations, respectively.
[c] Relative difference in primary thresholds between cluster systems, $Fe_n^+ \rightarrow Fe_{n-1}^+ + Fe$ and $Fe_{n-1}^+ \rightarrow Fe_{n-2}^+ + Fe$.
[d] Relative difference in thresholds within a cluster system, $Fe_n^+ \rightarrow Fe_{n-1}^+ + Fe$ and $Fe_n^+ \rightarrow Fe_{n-2}^+ + 2\ Fe$.
[e] Average of thresholds determined from analysis with Eq. (A7), $D^0(Fe_{n-1}^+-Fe) + \Delta E_0$(I), and ΔE_0(II), except for Fe_n^+ ($n = 3,4$), where ΔE_0(II) was not included, see the text.
[f] Analysis discussed in Ref. 8.

analyses of these clusters, are not changed by the lifetime considerations. Consequently, analysis is performed with Eq. (7) which yields $D^0(Fe_{n-1}^+-Fe)$. The values of N and E_0 used to model the data are summarized in Table I. The uncertainties in the BDEs arise from the uncertainty in N and the absolute uncertainty of the collision energy. The cross section for CID of Fe_2^+ has been previously published[8] and discussed in detail. Threshold analysis requires $N = 1.35 \pm 0.10$ and $E_0 = D^0(Fe_2^+) = 2.72 \pm 0.07$ eV. An excellent reproduction of the data from threshold to ~ 8 eV is provided.

The trimer cross section is also representative of analysis within this cluster size range. The best fit to the data from threshold to ~ 5.5 eV is found with $N = 1.6 \pm 0.10$, yielding $E_0 = 1.62 \pm 0.15$ eV. The use of $N = 1.6$ indicates that the rise from threshold is less sharp than observed in dimer CID and that cross section rises more linearly with increasing energy. Figure 5 shows the threshold region of the cross section, the model, and the model convoluted over the experimental energy distributions. A threshold enlargement shows the excellent fit of the data down to the noise level. Thus, $D^0(Fe_2^+-Fe) = 1.62 \pm 0.15$ eV, considerably weaker than $D^0(Fe^+-Fe)$.

The cross section for $Fe_4^+ + Xe \rightarrow Fe_3^+ + Fe + Xe$ also rises sharply from the noise allowing a precise threshold measurement. The threshold region is relatively short, approximately ~ 2 eV. Cross section analysis within this energy range uses $N = 1.6 \pm 0.15$ to best model the nearly linear rise from threshold. This form provides an excellent fit of the data to down the noise level, yielding $E_0 = 1.99 \pm 0.15$ eV, as demonstrated in Fig. 5. Comparatively, $D^0(Fe_3^+-Fe)$ is stronger than $D^0(Fe_2^+-Fe)$ but considerably weaker than $D^0(Fe^+-Fe)$.

Fe_n^+ ($n=5$–10): Threshold analysis. Comparison of all cross sections shows that CID processes of larger clusters share a common feature not observed with smaller clusters. This feature is apparent as a tail at low collision energies, as seen in the expanded views of Fe_6^+ and Fe_{10}^+ shown in Fig. 6 and as low energy shoulders in Fig. 4. The magnitudes are small, $<2\%$ of the main peak, but reproducible. Such features are suggestive of dissociative events with extra energy, such as those from kinetically or internally excited ions.

Conceivably, ions with different kinetic energies could be produced in two ways. Since the magnetic sector is a momentum analyzer, lower mass isotopomers with higher velocities could be passed in the same narrow momentum range as the primary isotopomers. The momentum analyzer resolution was carefully measured and is sufficiently high that the ion beam is composed of a single mass. That no kinetically hot ions are observed agrees with the narrow ion energy distribution expected from a supersonic expansion. Another means of obtaining ions of different kinetic energy is metastable decomposition of a larger cluster ion during flight from source to magnetic sector. Since ions are essentially monoenergetic through these regions, the parent and daughter ions should have nearly the same velocities, such that the daughter ions will have lower kinetic energies than ions emitted directly from the source. Careful retarding energy analysis of the ion beam confirms that the ion energy distribution is nearly Gaussian (~ 0.75 eV FWHM) and that no ions with kinetic energies in excess of this distribution are produced within 0.01%.

We have also performed experiments to determine possible effects of cluster internal energies. To increase the number of thermalizing collisions within the source, the He flow was increased from 5000 to 10 500 sccm. No changes in the thresholds were observed. As a check of excitation that occurs in the vaporization process, the average laser power was lowered from 28 to 20 W. No effect on the cross sections was observed, demonstrating that higher He flows or lower laser powers do not result in colder clusters. The latter is in contrast to Fe^+ formation, where the high laser power has been shown to create excited states.[42] This presumably indicates that cluster excited states are easier to collisionally quench

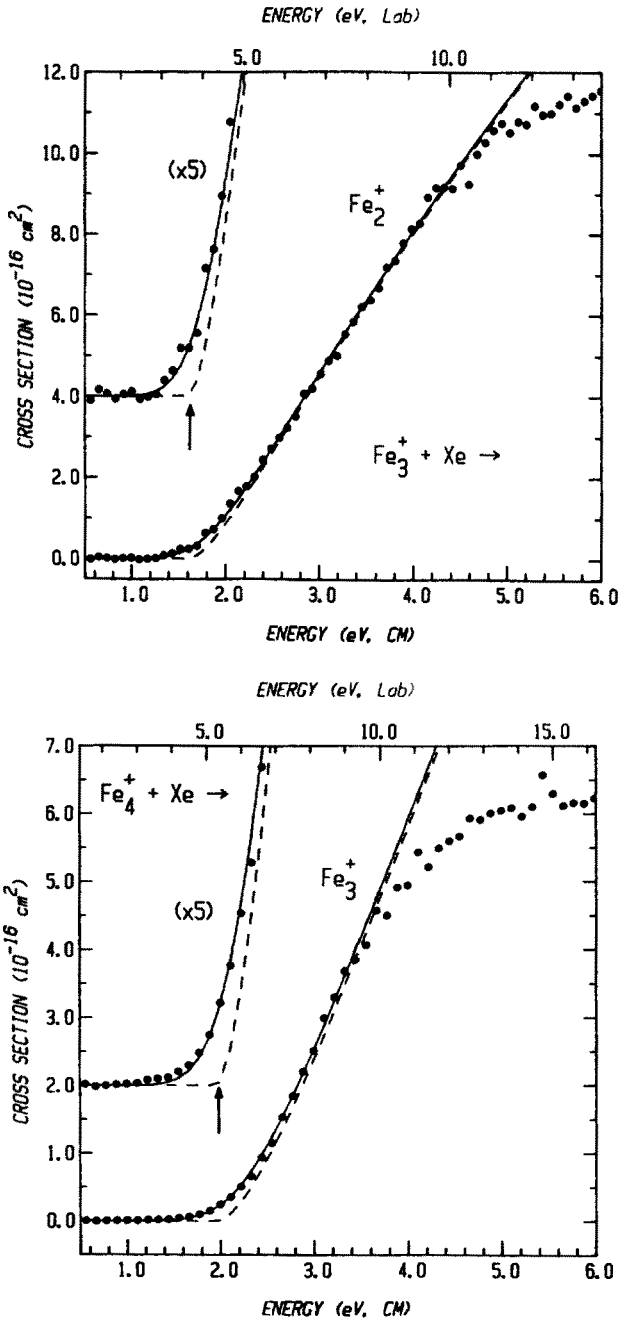

FIG. 5. CID cross section threshold energy dependence analyses for $Fe_n^+ + Xe \rightarrow Fe_{n-1}^+ + Fe + Xe$, $n = 3$ and 4. Cross section data (solid circles) are plotted as functions of collision energy in the center-of-mass (lower x axis) and laboratory (upper x axis) frames. An empirical model, Eq. (7) discussed in the text, is shown as a dashed line. The model convoluted with the experimental energy distributions is shown as a solid line. Arrows indicate dissociation thresholds obatined.

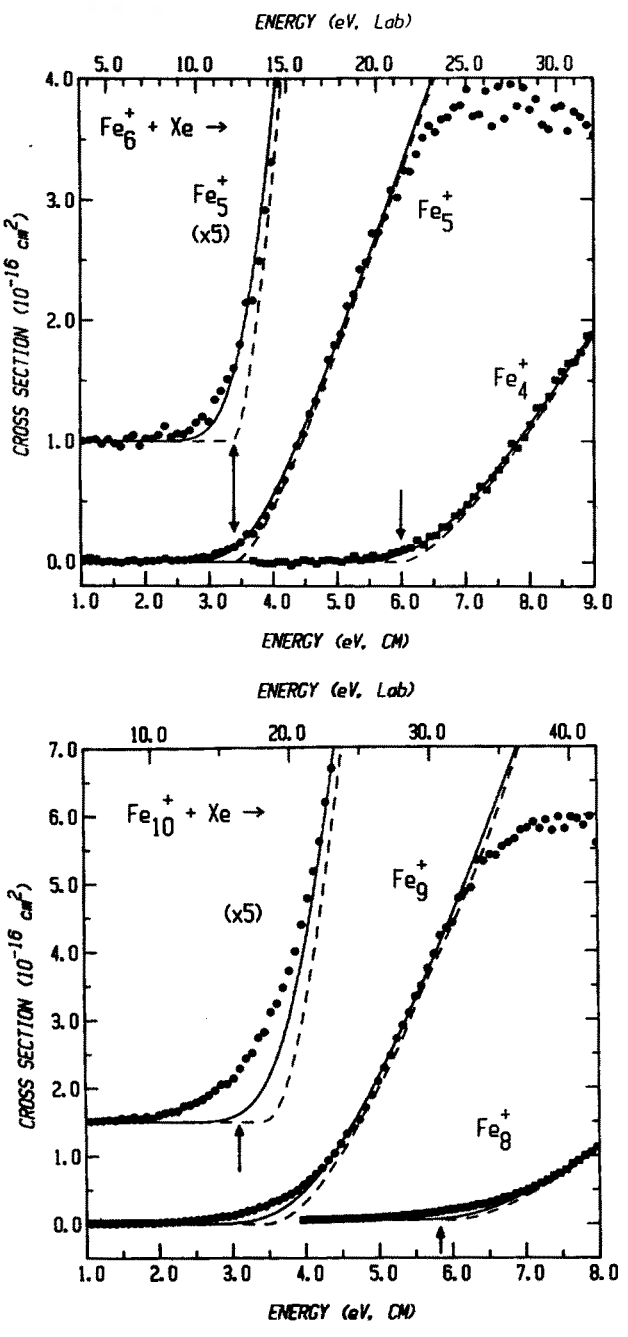

FIG. 6. CID cross section threshold energy dependence analyses for $Fe_n^+ + Xe \rightarrow Fe_{n-1}^+ + Fe + Xe$ and $\rightarrow Fe_{n-2}^+ + 2\ Fe + Xe$, $n = 6$ and 10. Cross section data for the primary (solid circles) and secondary (solid squares) product channels are plotted as functions of collision energy in the center-of-mass (lower x axis) and laboratory (upper x axis) frames. An empirical model, Eq. (A7) discussed in the text, is shown as a dashed line for each process. These models convoluted with the experimental energy distributions are shown as solid lines. Arrows indicate dissociation thresholds obtained.

than the atom, presumably due to their high state densities.

The supersonic expansion from the source helps to cool internal modes of the cluster. Although we cannot directly measure this cooling, an expansion of 220 Torr of pure Ar is sufficient to cause condensation to large Ar clusters. Addition of Ar (2.7%) to the main He flow forms the adduct, $Fe_n^+ \cdot Ar$, in low intensities, showing that some general cooling occurs. Collisions with Ar are also expected to quench internal excitation more effectively than He, because of the relatively high polarizability of Ar.[42] No changes were observed in the CID thresholds for Fe_n^+ upon addition of Ar to the flow.

There is also the possibility that cluster ions are collisionally reheated in the source or first two differential pumping regions. Indeed, if the ions are accelerated in the source region between the nozzle and skimmer, both the kinetic energy and internal energies of the cluster ions are affected. To avoid this, the source region is kept entirely field free.

However, to obtain sufficient ion intensities, ion lenses in the first (FSA) and second (FSB) differential pumping regions (DR1 and DR2) must be used to focus the ions. While voltages of up to 300 V on the FSB lenses have no affect on the CID thresholds, such large voltages on the FSA lenses do affect the appearance of the data. Hence, these voltages are held to less than 10 V as described in the experimental section. Note that since the background gas is He, 10 V corresponds to a center-of-mass collision energy of only 0.34 V for iron dimers and only 0.07 eV for iron decamers, much lower than the tails observed here. Further, there is only a 4% probability of a collision in this region (assuming a large collision cross section of 20 Å^2). While the possibility of collisional excitation cannot be ruled out completely, there is no evidence to suggest that it is responsible for the observed low energy tails, despite a careful evaluation of this possibility. Overall, we conclude that these threshold features are not attributable to clusters with excess internal excitation and that our ions are at least thermalized.

The effect of an oxygen impurity in the reactant gas was checked directly by conducting O_2 reactivity experiments. These indicate, however, that Fe_{n-1}^+ is not produced in the threshold regions of the present systems by such reactions.

One final possibility is that the low energy tails in the data are due to multiple collision events. This hypothesis has been verified by preliminary data which show systematic changes in the cross section energy dependence with Xe pressure variation. The energy dependences of the main portion of the cross sections are invariant with pressure, but the low energy portion increases with increasing Xe pressures. Thus, a small fraction of clusters ($\sim$1%) undergo multiple collisions with Xe. The low energy feature can be removed by extrapolating the pressure dependent portion of the cross sections to zero pressure. Quantitative pressure dependent experiments and analysis are underway and will be included in our paper on CID of larger Fe_n^+ clusters to more fully characterize this phenomenon.

$D^0(Fe_{n-1}^+$–Fe), n=5–10. Such a treatment of each cluster effectively quintuples the experimental work needed for the most accurate threshold determinations. As a prelude to this, the thresholds are determined by three means in this work. First, the pressure invariant portion of the threshold region is modeled, as for the smaller clusters. This analysis includes energies which range to $\sim$3–4 eV above threshold. Second, we also make use of relative thresholds for differently sized clusters to determine an E_0. For instance, by modeling the cross sections for $Fe_5^+ \rightarrow Fe_4^+ + Fe$ and $Fe_4^+ \rightarrow Fe_3^+ + Fe$ in exactly the same manner [by using Eq. (7) and keeping the value of N fixed at 1.5], a relative difference in BDEs can be obtained. Because $D^0(Fe_3^+$–Fe) is determined precisely as described above, the difference in thresholds provides $D^0(Fe_4^+$–Fe). These values determined from relative thresholds are more precise because the pressure effects should largely cancel and the same interpretation parameters are used. Third, independent measures of $D^0(Fe_{n-1}^+$–Fe) are provided by the relative thresholds for sequential CID processes for a single cluster size, $Fe_n^+ \rightarrow Fe_{n-1}^+ + Fe$ and $Fe_{n-2}^+ + 2$ Fe, in analogy with the extrapolated voltage method of determining ionization potentials. This difference should be an upper limit to the difference between $D^0(Fe_{n-1}^+$–Fe) and $D^0(Fe_{n-2}^+$–Fe), because kinetic shifts may cause loss of the second atom to be less efficient than the first.

An example of the analysis by these three means is outlined here for Fe_6^+ CID. First, the nearly linear energy dependence of the main portion of the cross section is best modeled by Eq. (A7) with $N = 1.60 \pm 0.15$ and $E_0 = 3.29 \pm 0.25$ eV. This threshold value includes a shift of $\sim$0.10 eV due to the lifetime considerations discussed above and in the Appendix. This model is shown in Fig. 6 and can be seen to reproduce the cross section nicely except at the very lowest energies in the expanded view. Second, the threshold of $Fe_6^+ \rightarrow Fe_5^+ + Fe$ is determined to be 0.97 ± 0.15 eV higher than the threshold for CID of the pentamer, $Fe_5^+ \rightarrow Fe_4^+ + Fe$. Since the latter bond energy is 2.50 ± 0.18 eV, this gives $D^0(Fe_5^+$–Fe) = 3.47 ± 0.23 eV. Third, the sequential dissociation processes $Fe_7^+ \rightarrow Fe_6^+ + Fe$ and $Fe_7^+ \rightarrow Fe_5^+ + 2$ Fe have thresholds that differ by 3.55 ± 0.25 eV. This value should also equal $D^0(Fe_5^+$–Fe). Averaging these three results and taking the pooled estimate of error, we report $D^0(Fe_5^+$–Fe) = 3.44 ± 0.18 eV.

Results of these analyses for Fe_n^+ (n = 5–10) are summarized in Table I. In the first method of analysis, N is found to be 1.5 to 1.7 for Fe_n^+ (n = 5–9), in good agreement with the proposed model for translationally driven endoergic reactions and that observed for Fe_n^+ (n = 2–4). Fe_{10}^+, however, requires $N = 1.9 \pm 0.2$, Table I. The effects of including the RRKM considerations are also given in Table I. These numbers are determined as discussed in the Appendix. For the second method of analysis, Fig. 7 shows the primary dissociation channels of all clusters normalized at their maxima. The relative thresholds agree qualitatively with results given in Table I. The third method of analysis is illustrated by Fig. 6, where the secondary thresholds are also

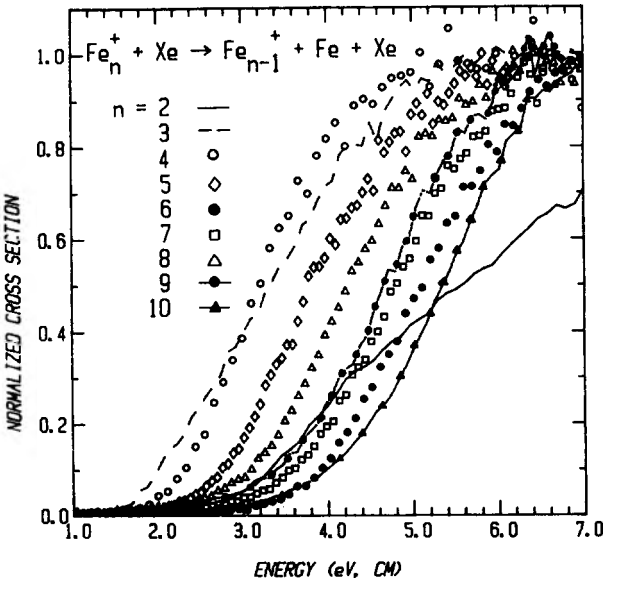

FIG. 7. Relative threshold behaviors of $Fe_n^+ + Xe \rightarrow Fe_{n-1}^+ + Fe + Xe$ for n = 2–10. Normalized cross sections are plotted as functions of collision energy in the center-of-mass frame (lower x axis).

shown. It can be seen that these threshold are nicely reproduced using the same means of analysis as the primary threshold (same value of N). Overall, the results of the three analysis procedures are in reasonably good agreement, and the final bond energy value cited is the average of all three determinations except for the smallest clusters ($n = 3$ and 4). Here the secondary thresholds are well in excess of the other determinations, presumably due to a combination of product channel competition, kinetic shifts, and angular momentum effects.

$D^0(Fe_{n-1}$–Fe), $n=2$–10. The BDE of a neutral iron cluster can be derived from the analogous ionic BDE and the difference of two ionization potentials via

$$D^0(Fe_n\text{–}Fe) = D^0(Fe_n^+\text{–}Fe) + IP(Fe_n) - IP(Fe_{n-1}). \quad (8)$$

The adiabatic ionization potentials for Fe_n ($n = 2$–10)[11] are used with the derived ionic BDEs to obtain the neutral BDEs, given in Table II. Cluster ions are found to be bound more strongly than their neutral counterparts. Fe_3^+ presents the only exception, as Fe_3 is more strongly bound by 0.15 eV. Fe_2^+ and Fe_5^+ are considerably more strongly bound than their neutral counterparts, whereas Fe_n^+ and Fe_n, $n > 5$ have practically equal BDEs. With these clusters, the higher ionic bond energies of ~0.1 eV may be attributable to stabilization by the attractive ion-induced dipole potential.[57]

C. Cluster bonding

Fe_2^+ is much more stable than Fe_3^+. This situation is reversed in the neutrals, where Fe_2 is considerably less stable than Fe_3. Also reversed are the neutral and ion binding energies of the dimer and trimer, $D^0(Fe_2^+) > D^0(Fe_2)$ and $D^0(Fe_2^+\text{–}Fe) < D^0(Fe_2\text{–}Fe)$. However, both Fe_2 and Fe_3 have sharp photoionization thresholds[11] (large Franck–Condon overlap) implying that the neutral and cationic clusters have similar bonding schemes. If the bond regions of the potential surfaces for the cation and neutral are similar, then the differences in the binding energies presumably result from differences in dissociation asymptotes. To examine the bonding further, we make use of simple promotion energy (PE) arguments as in our previous discussion of the dimer bonding.[8]

Dimers. Dissociation of Fe_2 ($4s\sigma^2 3d^{14}$) involves breaking a σ bond that results mainly from 4*s*–4*s* interactions.[6] Diabatic dissociation therefore occurs to two excited state atoms, 2 Fe*($4s^1 3d^7$), requiring a PE of 2·(0.86) eV. For Fe_2^+ ($4s\sigma^2 3d^{13}$), the situation is different, since diabatic dissociation can occur to $Fe^{+*}(4s^0 3d^7) + Fe(4s^2 3d^6)$ with a PE of only 0.23 eV. Fe_2^- ($4s\sigma^2 4s\sigma^{*1} 3d^{14}$), on the other hand, can dissociate to $Fe^-(4s^2 3d^7) + Fe^*(4s^1 3d^7)$, needing a PE of 0.86 eV. To compare $4s\sigma^2$ bond strengths, we calculate for each the sum of the BDE and the PE, the diabatic dissociation energy (DDE). Thus, the DDEs of the neutral, cationic, and anionic dimers are 2.84, 2.95, and 2.73 eV, respectively. The near equality of the DDEs is consistent with a strong 4*s*–4*s* σ bond, with some 3*d*–3*d* bonding interations in all three.

Trimers. Since the sharpness of the Fe_3 photoionization threshold implies that the neutral and cation have similar bonding, simple PE arguments may also be useful in understanding Fe_3 and Fe_3^+. We do this by comparing the energy required for diabatic dissociation of the trimers to three atoms (which we also term DDE). Thus, the DDE of Fe_3 is the energy required to dissociate to the ground state dimer and an atom with PE′ plus the DDE of Fe_2, $D^0(Fe_2\text{–}Fe) + PE' + DDE(Fe_2) = 1.79 + PE' + 2.84 = 4.63$ eV + PE′. Likewise, $DDE(Fe_3^+) = D^0(Fe_2^+\text{–}Fe) + PE'' + DDE(Fe_2^+) = 1.64 + PE'' + 2.95 = 4.59$ eV + PE″. Since the bonding in Fe_3 and Fe_3^+ are similar, we expect the DDEs to be nearly the same, which in turn implies that PE′ = PE″. This means that equivalent Fe atoms are added to Fe_2 and Fe_2^+ to make the respective trimers. Note that if Fe_3^- has a similar bonding scheme as the cation and neutral (the same DDE and PE), then these simple PE arguments suggest that $D^0(Fe_2^-\text{–}Fe) \simeq 4.6 - 2.7 \simeq 1.9$ eV.

If the trimer bonding is dominated by interactions of 4*s*

TABLE II. Ionic and neutral bond dissociation energies.

n	$D^0(Fe_{n-1}^+\text{–}Fe)$[a] (eV)	$IP(Fe_n)$[b] (eV)	$D^0(Fe_{n-1}\text{–}Fe)$[c] (eV)	$\sigma(Fe_{n-2}^+)/\sigma(Fe_{n-1}^+)$[d]
1	...	7.902(0.0002)[e]	...	...
2	2.72(0.07)	6.30 (0.01)	1.12(0.07)	...
3	1.64(0.15)	6.45 (0.05)	1.79(0.16)	*N*
4	1.99(0.15)	6.40 (0.10)	1.94(0.19)	*Y*
5	2.50(0.18)	5.95 (0.05)	2.05(0.21)	*N*
6	3.44(0.18)	5.90 (0.10)	3.39(0.21)	*Y*
7	3.26(0.21)	5.75 (0.05)	3.11(0.24)	*N*
8	2.74(0.23)	5.65 (0.05)	2.64(0.24)	*Y*
9	2.88(0.27)	5.45 (0.05)	2.68(0.28)	*Y*
10	3.10(0.35)	5.37 (0.10)	3.02(0.37)	*S*

[a] Derived in this work.
[b] Values given in eV. From Ref. 11, except where noted.
[c] Derived from ionic binding energies and cluster ionization potentials using Eq. (8) in the text. Uncertainties are in parentheses.
[d] Comparison of $\sigma(Fe_{n-2}^+)$ and $\sigma(Fe_{n-1}^+)$ magnitudes at a center-of-mass collision energy of 25 eV. For the ratio $\sigma(Fe_{n-2}^+)/\sigma(Fe_{n-1}^+)$, *Y* denotes > 1, *N* denotes < 1 at all energies, and *S* denotes = 1.
[e] Ref. 61.

orbitals, then a simple analogy can be made to the familiar H_3 and H_3^+ systems. In the triangular molecule H_3^+,[58] the two electrons occupy a bonding MO that lies below two degenerate antibonding MOs. In the linear H_3 molecule, these two degenerate orbitals have split in energy, so that the third electron occupies what has become a largely nonbonding orbital. The linear structure is also most favorable for H_3^-, since the nonbonding orbital becomes doubly occupied with addition of the fourth electron.

For the case of the iron trimers, we now need to find the number of 4*s* electrons involved in the bonding. The promotion energy arguments suggest that the cation and neutral dimers both have two 4*s* electrons and that formation of the cation and neutral trimers involves addition of an atom in the same state, i.e., having the same PE. If a ground state $Fe(4s^23d^6)$ atom is added then both trimers will have four 4*s* electrons. On the other hand, if $Fe^*(s^13d^7)$ atoms are added to the dimers, requiring PEs of 0.86 eV, both have three 4*s* electrons. Either possibility suggests that the cation and neutral trimer should have linear structures in analogy with H_3 and H_3^-.

This line of reasoning was initiated by the relatively large cross section for dissociation of Fe_3^+. For Fe_3^+, the least compact structure is a linear structure. In preliminary reactive studies of small iron cluster ions with O_2,[59] we find that Fe_3^+ has a relatively large reaction cross section, also indicating its weak bond and possibly an unusually reactive structure. It will be interesting to test these ideas as structural information on all the trimers becomes available.

Despite the appealing, but probably naive simplicity of the approach above, more involved calculations have generally found that the neutral trimer is triangular. An early calculation on the structure and BDEs of Fe_3 assumed bond lengths equal to the bulk atomic radius (2.48 Å) and that Fe_3 is low spin,[9] i.e., having substantial 3*d*–3*d* bonding interactions. Since this time, the Fe_2 bond length, which may be a better measure of the Fe_3 bond lengths, has been measured by EXAFS as 2.02 Å.[60] Nevertheless, the triangular structure was found to be the most stable. In a more recent study, SCF-$X\alpha$ scattered wave MO calculations were performed on Fe_2 and Fe_3, reproducing both IPs and the experimental Fe_2 bond length. The most stable configuration for Fe_3 is predicted to be triangular. The calculations find the the spin-polarized state of Fe_3 is the most stable, implying that 3*d* electrons play a role in the bonding of Fe_3.

Larger clusters. All Fe_n^+ and Fe_n ($n > 3$) have similar BDEs except for $n = 5$, where $D^0(Fe_4^+-Fe)$ is 0.45 eV larger than $D^0(Fe_4-Fe)$. Therefore as for the trimer, the similar BDEs suggest that formation of the ionic and neutral clusters requires a similar PE. In contrast, the difference in Fe_5^+ and Fe_5 BDEs suggests that these clusters require atoms with different promotion energies, as for the dimers. However, the bonding in the cation and neutral clusters larger than the trimer may not be identical, since the experimental photoionization thresholds are much less sharp than those of Fe_2 and Fe_3.[11] Consequently, promotion energy arguments cannot be used quantitatively for these clusters.

D. Size-dependent trends

The binding energy dependence on cluster size is not as smooth as that of the ionization potentials.[11] Both the neutral and ionic BDEs derived in this work and the known IPs are shown in Fig. 8. Fe_2^+ is fairly strongly bound, while in contrast, Fe_3^+ has the weakest BDE of any cluster studied here. As cluster size increases, the BDEs increase to a maximum at $D^0(Fe_5^+-Fe)$. The BDEs decrease to a local minimum at Fe_8^+, then rise to $D^0(Fe_9^+-Fe) = 3.10$ eV. The neutral BDEs also do not show a smooth variation with size. Fe_2 has the weakest binding energy, and a local minimum in

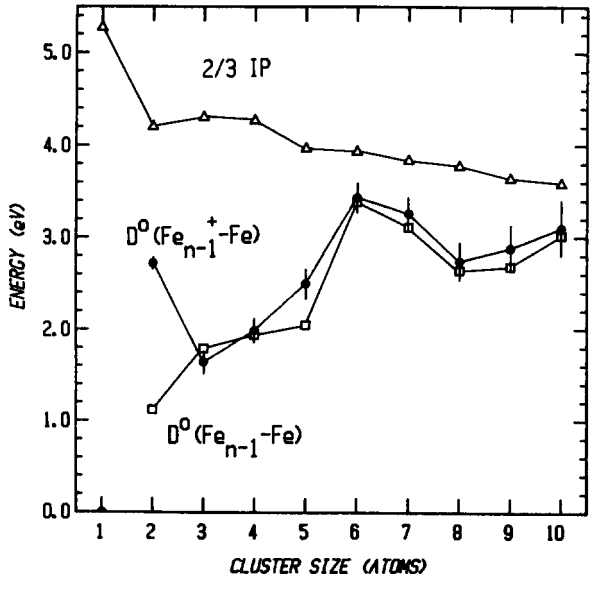

FIG. 8 $D^0(Fe_{n-1}^+ - Fe)$ (solid circles) and $D_0(Fe_{n-1}-Fe)$ (open squares), derived in this work, plotted as a function of cluster size. IP(Fe_n) (open triangles, scaled down by a factor of 2/3) from Ref. 11 are also shown.

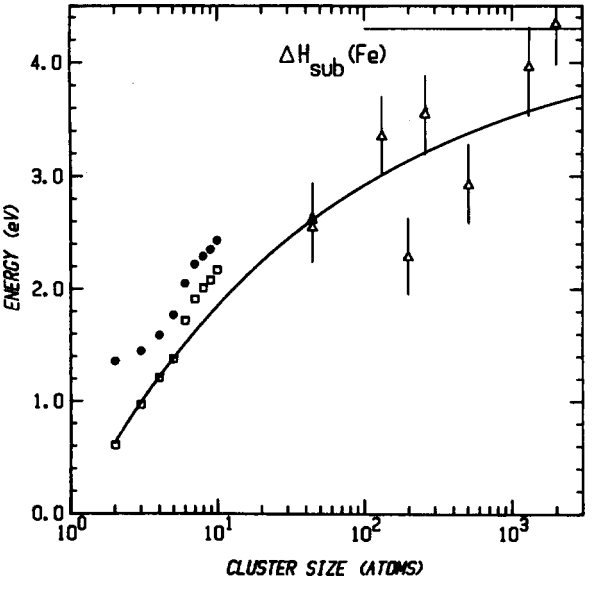

FIG. 9. The binding energy per atom of Fe_n^+ (solid circles) and Fe_n (open squares) as a function of cluster size. Also shown is data from Ref. 60 derived from homogeneous nucleation studies (open triangles) and an empirical model, Eq. (9), used to show convergence to ΔH_{sub} (Fe, *s*), which is shown as a line.

BDEs is found at Fe_8. Also similar to the ions, $D^0(Fe_5\text{–}Fe)$ represents the maximum BDE found.

Further increases in both the ion and neutral BDEs are expected with larger clusters, since cluster BDE per atom must eventually converge to the bulk enthalpy of sublimation, 4.30 eV.[61] The BDE per atom, plotted in Fig. 9, does show a smooth increase from Fe_2^+ (1.36 eV) to Fe_{10}^+ (2.43 eV). The same general behavior is noted for the neutral cluster BDEs. The neutral per atom binding energy starts lower than the ionic BDEs, due to the relative dimer bond strengths. With increasing cluster size, these two curves rise and begin to converge, as expected as the effects of the ionic charge lessen.

From these results, it is clear that BDE/atom does not converge to ΔH_{sub} in this cluster size range, but that convergence apparently occurs with much larger clusters. It will be interesting to extend these studies to larger clusters, since this quantity might be expected to change dramatically for $n = 14$–15, where evidence for a structural change was found by Richtsmeier *et al.*[12] The slow convergence to the bulk is in qualitative agreement with a formula previously proposed for the binding energies per atom,[62]

$$E_0(\text{atomic})/n = \Delta H_{sub}(1 - n^{-0.25}), \quad (9)$$

where E_0(atomic) is the energy required for complete atomization of the cluster, calculated by Eq. (4). Equation (9) was derived from experimental work on the homogeneous condensation of supersaturated Fe vapor to large clusters of 10^2 to 5×10^3 atoms and, since no data was available on the binding energies of small iron clusters, from previous calculations on small clusters of a variety of metals. The calculations include those for small neutral iron clusters.[9] The effectiveness of this simple formula in reproducing our data as well as that for much larger clusters is rather remarkable. This good agreement suggests that Eq. (9) may provide reasonable approximations to the binding energies of both small and large clusters of iron and other metals.

E. Dissociation mechanism

Except for the primary processes, the neutral CID products and the dissociation mechanism must be identified by their thresholds and general cross section features. The expected thresholds for these product channels are calculated from the neutral and ionic BDEs listed in Table II via Eq. (6) and are listed in Table III. For clusters larger than five atoms, only thresholds for fragmentation to atomic neutral products are given, due to the large numbers of available pathways.

Fe_3^+. For CID of Fe_3^+, the first system where two ionic products can be produced, the threshold of $\sigma(Fe^+ + Fe_2)$ should lie higher than the threshold for the primary product

TABLE III. Energy thresholds for Fe_n^+ CID product channels.[a]

System	Product channel	E_0	System	Product channel	E_0
Fe_2^+	$Fe^+ + Fe$	2.72	Fe_7^+	$Fe_6^+ + Fe$	3.26
Fe_3^+	$Fe_2^+ + Fe$	1.64		$Fe_5^+ + 2\ Fe$	6.7
	$Fe^+ + Fe_2$	3.2		$Fe_4^+ + 3\ Fe$	9.2
	$Fe^+ + 2\ Fe$	4.3		$Fe_3^+ + 4\ Fe$	11.2
Fe_4^+	$Fe_3^+ + Fe$	1.99	Fe_8^+	$Fe_7^+ + Fe$	2.74
	$Fe_2^+ + Fe_2$	2.5		$Fe_6^+ + 2\ Fe$	6.0
	$Fe_2^+ + Fe + Fe$	3.6		$Fe_5^+ + 3\ Fe$	9.4
	$Fe^+ + Fe_3$	3.4		$Fe_4^+ + 4\ Fe$	11.9
	$Fe^+ + Fe_2 + Fe$	5.2		$Fe_3^+ + 5\ Fe$	13.9
	$Fe^+ + 3\ Fe$	6.3		$Fe_2^+ + 6\ Fe$	15.6
Fe_5^+	$Fe_4^+ + Fe$	2.50	Fe_9^+	$Fe_8^+ + Fe$	2.88
	$Fe_2^+ + Fe_3$	3.2		$Fe_7^+ + 2\ Fe$	5.6
	$Fe_3^+ + Fe_2$	3.4		$Fe_6^+ + 3\ Fe$	8.9
	$Fe_3^+ + 2\ Fe$	4.5		$Fe_5^+ + 4\ Fe$	12.3
	$Fe_2^+ + Fe_2 + Fe$	3.5		$Fe_4^+ + 5\ Fe$	14.8
	$Fe_2^+ + 3\ Fe$	6.1			
	$Fe^+ + Fe_4$	4.0	Fe_{10}^+	$Fe_9^+ + Fe$	3.10
	$Fe^+ + Fe_3 + Fe$	6.0		$Fe_8^+ + 2\ Fe$	6.0
	$Fe^+ + Fe_2 + Fe_2$	6.6		$Fe_7^+ + 3\ Fe$	8.7
	$Fe^+ + Fe_2 + 2\ Fe$	7.7		$Fe_6^+ + 4\ Fe$	12.0
	$Fe^+ + 4\ Fe$	8.8		$Fe_5^+ + 5\ Fe$	15.4
				$Fe_4^+ + 6\ Fe$	17.9
Fe_6^+	$Fe_5^+ + Fe$	3.44			
	$Fe_4^+ + 2\ Fe$	5.9			
	$Fe_3^+ + 3\ Fe$	7.9			
	$Fe_2^+ + 4\ Fe$	9.6			

[a] Thresholds in eV. These values are derived by using the neutral and ionic binding energies listed in Table II.

channel, $Fe_2^+ + Fe$, by $D^0(Fe_2^+) - D^0(Fe_2) = 1.60$ eV, as given in Table II. This value is known accurately because it is also the difference in ionization potentials, $IP(Fe)^{63} - IP(Fe_2)$. As a result, $\sigma(Fe^+ + Fe_2)$ should have a threshold of $1.64 + 1.60 = 3.24$ eV. Likewise, the threshold of $\sigma(Fe^+ + 2\ Fe)$ is even higher by $D^0(Fe_2) = 1.12$ eV and should occur at 4.36 eV. The data in Fig. 4 clearly show that dissociation to $Fe^+ + Fe_2$ does not begin near 3.2 eV, but that the threshold of about 5 eV is in better agreement with the threshold for dissociation to $Fe^+ + 2$ Fe. Thus the thresholds imply that Fe^+ production is accompanied by loss of two Fe atoms.

A threshold that is shifted to higher energies can result from a kinetic shift, due to high product kinetic energies. While this possibility cannot be completely ruled out, an additional piece of evidence further suggests that $Fe^+ + 2$ Fe is the dominant pathway for Fe^+ formation. This is the observation that the gain in Fe^+ production is exactly mirrored by the loss in Fe_2^+ product intensity, such that σ_{tot} remains constant.

One reason for the inefficiency of the $Fe^+ + Fe_2$ product channel is competition with the $Fe_2^+ + Fe$ product channel. Since these two processes differ only in the location of the charge, relative IPs are important in determining branching ratios. Fe_2^+ formation is favored over Fe^+ production substantially upon cleavage of Fe_3^+, because $IP(Fe_2)$ is considerably lower than $IP(Fe)$, $\Delta IP = 1.60$ eV. This effectively leaves one route for Fe^+ formation: fragmentation of Fe_2^+.

Fe_4^+. The threshold for $Fe_4^+ \rightarrow Fe_3^+ + Fe$ is 1.99 eV. The other two cross sections, $\sigma(Fe_2^+)$ and $\sigma(Fe^+)$, have apparent thresholds of 3.5 and 7 eV, respectively. The two dimer ion formation processes, $\sigma(Fe_2^+ + Fe_2)$ and $\sigma(Fe_2^+ + 2\ Fe)$, have calculated thresholds of 2.5 and 3.6 eV, respectively. Fe_2^+ is not observed near 2.5 eV, indicating $Fe_4^+ \rightarrow Fe_2^+ + Fe_2$ does not occur near threshold. Instead, the agreement with the higher threshold implies that $Fe_4^+ \rightarrow Fe_2^+ + 2$ Fe is the dominant process for dimer ion formation. Turning to Fe^+ production, we see that Fe^+ can be formed via three different neutral products: 3 Fe, $Fe_2 + Fe$, and Fe_3. These have expected apparent thresholds of 6.3, 5.2, and 3.6 eV, respectively. The experimental threshold agrees with the highest threshold, indicating that the mechanism for Fe^+ formation is loss of three neutral atoms. *A priori*, we would expect the $Fe^+ + Fe_3$ dissociation pathway to be effectively blocked, because of the competition of the $Fe_3^+ + Fe$ product channel, favored by $\Delta IP = 1.42$ eV. In contrast, production of Fe_2^+ is not in direct competition with Fe_3^+ production.

A mechanism for Fe_4^+ dissociation by sequential loss of Fe atoms is also supported by the relative cross section behaviors, as with CID of the Fe_3^+. With molecular fragmentation, σ_{tot} might be expected to increase if a new channel for Fe^+ production becomes energetically accessible, such as the $Fe_2^+ + Fe_2$ channel. Instead, as $\sigma(Fe_2^+)$ rises, $\sigma(Fe_3^+)$ peaks and then declines. Similarly with increasing energies, as $\sigma(Fe^+)$ increases, the rise in $\sigma(Fe_2^+)$ slows. This behavior combined with the flat total cross section demonstrates the one-to-one correspondence between the gain in one cross section and a loss in another, providing solid evidence that the primary dissociation pathway is sequential loss of Fe atoms.

Fe_n^+ ($n=5$–10). The pentamer can form four ionic products. If accompanied by loss of neutral iron atoms, the Fe_3^+, Fe_2^+, and Fe^+ cross sections should have thresholds at 4.5, 6.1, and 8.8 eV, respectively. The agreement with the apparent experimental thresholds of 4.5, 6.5, and ~12 eV, again suggests a mechanism for product formation of sequential loss of Fe atoms. The $\sigma(Fe^+)$ threshold is quite a bit higher than expected, presumably due to the extremely low Fe^+ intensities or a kinetic shift. The marked decrease in $\sigma(Fe_4^+)$ that accompanies the rise in $\sigma(Fe_3^+)$ clearly shows the parental nature of Fe_4^+. Fe_3^+ decomposition to Fe_2^+ is not as evident, due to the small cross section for Fe_2^+ formation.

Fe_n^+ of six to ten atoms have similar behaviors to the systems discussed above. The thresholds best agree with the thresholds expected for sequential loss of Fe atoms. No evidence for formation of molecular neutral fragments is found. Apparent thresholds are found to be higher than the threshold energies calculated using Table I. The difference becomes larger with increasing cluster size and for smaller product ions, suggestive of kinetic shifts. Such shifts are reasonable for processes where the internal energy available for dissociation is lost as Fe product translation. This holds in these cases, where product ion formation requires sequential loss of Fe atoms.

F. Branching ratios

In mass spectrometry, product ion branching ratios at high energies can give relative stabilities of the fragment ions, assuming that the fragments originate from a common precursor. Although consideration must be given to the dynamic effects, such as angular momentum conservation,[64] we may expect that the relative cross sections magnitudes also reflect relative product ionization potentials and relative product stabilities.

Comparison of the Fe_{n-1}^+ and Fe_{n-2}^+ product branching ratios shows that neither product is the dominant dissociation channel for all clusters. Instead, for Fe_n^+, $n = 4$, 6, 8, and 9, $\sigma(Fe_{n-1}^+)$ is favored over $\sigma(Fe_{n-2}^+)$ at lower energies, but by 15 eV, $Fe_n^+ \rightarrow Fe_{n-2}^+ + 2$ Fe becomes the most probable product channel. This behavior is not noted for Fe_n^+, $n = 3$, 5, and 7. Rather, $\sigma(Fe_{n-1}^+)$ remains larger than $\sigma(Fe_{n-2}^+)$ over the entire energy range. For $n = 10$, $\sigma(Fe_{n-1}^+)$ and $\sigma(Fe_{n-2}^+)$ are equally probable at higher energies. The cluster size dependence of this branching ratio is summarized in Table II.

The dominant fragment at low energies is Fe_{n-1}^+, due to thermodynamic considerations, but at high energies, the branching ratios show a general correlation with relative fragment BDEs. For Fe_n^+, $n = 4$, 8, and 9, the Fe_{n-2}^+ fragment is found to be more strongly bound than the Fe_{n-1}^+ fragment. For this reason, the Fe_{n-1}^+ product can easily fragment to $Fe_{n-2}^+ + Fe$, transferring intensity from $\sigma(Fe_{n-1}^+)$ to $\sigma(Fe_{n-2}^+)$, as the data indicate. Conversely, for clusters,

$n = 3$, 5, and 7, the Fe_{n-1}^+ fragment is relatively strongly bound. This stability causes Fe_{n-1}^+ to be the most probable product throughout the energy range. The equality of the branching ratio for Fe_{10}^+ shows that loss of one and two atoms become equally probable implying that the fragments have nearly equal BDEs. In agreement, analysis shows that the nanomer and octomer ion BDEs differ only slightly (0.1 eV). Fe_6^+, the most strongly bound cluster ion, presents an exception as the Fe_4^+ fragment is favored, even though less strongly bound than the Fe_5^+ fragment.

G. Comparison to previous work

Previous determinations of iron cluster binding energies have centered around the neutral dimer. These studies have given $D^0(Fe_2)$ ranging from 0.68 to 1.35 eV, or $D^0(Fe_2^+) = 2.15$ to 2.82 eV, if known IPs are incorporated. Previously, only two studies have made determinations of the Fe_2^+ BDE, not including our Fe_2^+ study.[8] Jacobson and Freiser used photodissociation of Fe_2^+ in an ICR cell to measure $D^0(Fe_2^+) = 2.68$ eV.[65] Later, Brucat *et al.* (BZPYS)[52] employed photofragmentation to dissociate jet-cooled Fe_2^+ and set limits of $2.43 \leqslant D^0(Fe_2^+) \leqslant 2.92$ eV. We find that the dimer ion BDE is $D^0(Fe_2^+) = 2.72 \pm 0.07$ eV, in excellent agreement with both past results.

The only BDE values for Fe_n^+ ($n > 2$) available are those determined by BZPYS, $D^0(Fe_{n-1}^+\text{–Fe}) < 2.33$ eV, $n = 4$–10. For Fe_3^+, BZPYS were able to determine a somewhat narrower range of $1.17 \leqslant D^0(Fe_2^+\text{–Fe}) \leqslant 2.18$ eV. Our value of $D^0(Fe_{2\text{-Fe}}^+) = 1.64 \pm 0.15$ eV fits nicely between these bounds. In contrast, for clusters larger than Fe_4^+, our BDEs are somewhat higher than the limiting value of 2.33 eV. This upper limit was determined by assigning the dissociation of the cluster to one-photon (2.33 eV) events. As a result, discrimination of single photon from multiphoton processes is essential in providing correct limits. Our results clearly suggest that multiphoton processes are involved. A two-photon event, although unlikely, deposits 4.66 eV into the cluster, and hence should have a relatively large cross section for dissociation. Since the fluence dependence studies used to distinguish one- and two-photon events are quite difficult, it seems probable that the photodissociation limits are in error.

BZPYS found that lowest energy pathway to photodissociation was by loss of an Fe atom from the cluster and that further fragmentation proceeds via loss of more Fe atoms. This mechanism is precisely the same as determined here. The congruent dissociation mechanisms suggests that both collisionally activated and photoexcited clusters have rapid equilibration of energy into internal modes followed by dissociation to ground state products.

V. CONCLUSIONS

A new guided ion beam instrument is described in detail. This apparatus is used to make and study mass-selected, thermalized, bare transition metal cluster ions. Interaction of the cluster with a neutral gas occurs within an octopole ion guide, allowing accurate measurement of metal cluster reaction cross sections over a wide range of well-defined interaction energies.

In this paper, we report the first use of ion beam techniques for measurement of transition metal cluster ion binding energies for species larger than the dimer. The energy dependences of collision-induced dissociation of singly charged iron cluster cations from 2 to 10 atoms with Xe are studied. With each, the dissociation pathway of lowest energy is loss of one iron atom from the cluster. With increasing collision energies, further dissociation occurs by loss of successive iron atoms, an evaporative mechanism. No evidence for fission to neutral molecular fragments is observed. Ion cluster BDEs, $D^0(Fe_{n-1}^+\text{–Fe})$, are obtained from cross section threshold analysis. By using known ionization potentials, neutral BDEs are also derived. Branching ratios also provide information on relative fragment stabilities and the mechanism for dissociation.

Current efforts in our laboratory are aimed at extending these binding energy determinations to larger Fe_n^+ clusters, $n = 11$–18 and a number of other transition metal ion clusters including: Nb_n^+, V_n^+, and Co_n^+. In future work, we plan to explore the reactivity of ligated and bare transition metal clusters both in terms of quantitative thermochemistry and qualitative periodic trends.

ACKNOWLEDGMENTS

This work is supported by the Army Research Office, DAAL03-87-2211, and the instrument was constructed with funds from the Department of Defense University Research Instrumentation Program. Early instrumental development was made possible by support from Exxon and the Research Corp. D.A.H. thanks the National Science Foundation for a Graduate Fellowship. The authors thank: Terrence Lee, Raymond Lee, and David Suchard for their valued assistance in instrument construction and the U.C. Berkeley Chemistry machine and electronics shops for their assistance. We note the generosity of Varian and Assoc. for donating the magnetic iron used for magnet pole modifications and Cooper Laser Sonics, Plasma Kinetics for donating the unstable resonator laser optics.

APPENDIX: STATISTICAL MODELING OF COLLISION-INDUCED DISSOCIATION THRESHOLDS

RRKM theory can provide an energy-dependent unimolecular rate constant for dissociation. We outline a method of data analysis that uses an empirical form and the probability derived from this rate to model the threshold behaviors of collision-induced dissociation cross sections. The resulting model is designed to model reactions of the type given by

$$Fe_n^+ \rightarrow Fe_{n-1}^+ + Fe. \tag{A1}$$

The usual form of the RRKM unimolecular rate constant is shown in[56]

$$k(E - E_0) = s\frac{Q^+ N^+(E - E_0)}{Q \quad h\rho(E)}, \tag{A2}$$

where $N^+(E - E_0)$ is the sum of states of the transition state at the energy above the dissociation energy $(E - E_0)$ and

$\rho(E)$ is the reactant density of states at the total energy E. Q^+ and Q are the rotational partition functions of the transition state and the energized cluster, respectively. In this work, we do not explicitly consider the rotational contributions (i.e., $Q = Q^+$). The reaction pathway degeneracy s is assumed to be equal to n, the number of atoms in the cluster. This assumption should be good for small clusters in which all atoms are "surface" atoms.

To evaluate the rate expression, vibrational frequencies of the transition state and reactant must be known or calculable. Since these frequencies have yet to be measured for iron clusters larger than the dimer, we use a method outlined by Jarrold and Bower (JB),[54] where the vibrational frequencies are obtained from the Debye model of solid state physics and the dimer frequency. This treatment is untested, but it yields the distribution of frequencies needed for the calculation and appears to be a reasonable starting point. The reaction coordinate is taken as the median frequency and two neighboring frequencies in the distribution are halved, to account for transitional modes as previously suggested by JB. For Fe, the Debye frequency is $\nu_D = 292\ \text{cm}^{-1}$.[66] We estimate the ion dimer frequency as 350 cm^{-1} from the known Fe_2 value of 300 cm^{-1},[7(a)] since the ion dimer BDE is considerably stronger than the neutral dimer BDE. The results of these calculations are shown in Fig. 3 for various cluster sizes and for the case where $E_0 = 2$ eV.

Now we wish to modify the empirical threshold model, given by Eq. (7) in the text, since it has proven to be quite useful in modeling atomic and dimer ion reactions with numerous neutral molecules. Forms of this nature can be derived by using

$$\sigma(E) = \int_0^{b_{\max}} 2\pi \cdot \Omega(E) \cdot b\, db, \tag{A3}$$

$\Omega(E)$ is the opacity function, which represents a probability for reaction to occur and b is the impact parameter. For instance, in the simple line-of-centers (LOC) model,[67] the relative reactant velocities (and energy) must be nonzero after surmounting the thermodynamic and centrifugal barriers for reaction to occur. As a result, b must satisfy the relation $E - E_0 - E(b/d)^2 \geqslant 0$, where d is the distance of closest approach of the rare gas atom and the cluster. If b_{max} is defined as the largest impact parameter for reaction, then $b_{\max}^2 = d^2 \cdot (E - E_0)/E$. Evaluation of Eq. (A3) ($\Omega = 1$) yields $\sigma_{\text{LOC}} = \pi d^2 \cdot (E - E_0)/E$, equivalent to Eq. (7) where $N = 1$ and $\sigma_0 = \pi d^2$.

In a more generalized model, it is *assumed* that b^2 takes on a form that is very similar to the simple model above, namely,

$$b^2 = d^2 \cdot (E - \Delta E - E_0)^N / E. \tag{A4}$$

Here, the quantity $E - \Delta E$ is the energy that is actually transferred into the internal energy of the cluster by a collision with an energy E. Equivalently, ΔE is the energy that remains in relative translational motion. The amount of internal energy imparted to the cluster is governed (at least in part) by the impact parameter. For instance, grazing collisions (large values of b) result in small values of $E - \Delta E$, while small impact parameters lead to the largest values of internal energy. We relate these quantities via Eq. (A4) and note that the integration over b in Eq. (A3) can be replaced by an integration over ΔE. To do this, we differentiate Eq. (A4) to obtain

$$\begin{aligned} d(b^2) &= 2b\, db \\ &= -N \cdot d^2 \cdot [(E - E_0 - \Delta E)^{N-1}/E]\, d\Delta E. \end{aligned} \tag{A5}$$

We next need to evaluate $\Omega(E)$, the probability that dissociation occurs at a given value of b (or ΔE) and E. Since the internal energy of the cluster is $E - \Delta E$, the RRKM rate constant for dissociation is given by Eq. (A2) as $k(E - \Delta E - E_0)$. Combined with the time available for dissociation, τ, the rate constant gives the probability for dissociation described by

$$P(E) = 1 - \exp[-k(E - E_0 - \Delta E) \cdot \tau]. \tag{A6}$$

We equate this probability with $\Omega(E)$.

Substituting Eqs. (A5) and (A6) into Eq. (A3) yields

$$\sigma(E) = \frac{\pi d^2 N}{E} \int_0^{E - E_0} (E - E_0 - \Delta E)^{N-1} [1 - \exp\{-k(E - \Delta E - E_0) \cdot \tau\}] \cdot d\Delta E. \tag{A7}$$

Essentially, this cross section is a convolution of the empirical form with the RRKM probability for dissociation on a time scale τ. As must be the case, Eq. (A7) does reduce to Eq. (7), the form without RRKM considerations, when the rate constant is high ($> 10^6$/s, as for small clusters), when the collision energies (E) are large, or at longer interaction times (large τ, although this quantity cannot be changed easily in these experiments). In these cases, threshold analysis with Eq. (A6) is equivalent to analysis with Eq. (7).

[1] T. G. Dietz, M. A. Duncan, D. E. Powers, and R. E. Smalley, J. Chem. Phys. **74**, 6511 (1981).
[2] V. E. Bondybey and J. H. English, J. Chem. Phys. **76**, 2165 (1982).
[3] E. A. Rohlfing, D. M. Cox, and A. Kaldor, J. Chem. Phys. **88**, 4497 (1986); D. E. Powers, S. G. Hansen, M. E. Geusic, D. L. Michalopoulos, and R. E. Smalley, *ibid.* **78**, 2866 (1983).
[4] M. D. Morse, Chem. Rev. **86**, 1049 (1986).
[5] C. W. Bauschlicher, Jr., S. R. Langhoff, and P. R. Taylor, J. Chem. Phys. **88**, 1041 (1988); S.R. Langhoff and C. W. Bauschlicher, Jr., *ibid.* **85**, 7211 (1986).
[6] (a) M. Tomonari and H. Tatewaki, J. Chem. Phys. **88**, 1828 (1988); (b) D. G. Leopold, J. Almlof, W. C. Lineberger, and P. R. Taylor, *ibid.* **88**, 3780 (1988); (c) I. Shim and K. A. Gingerich, *ibid.* **77**, 2490 (1982); (d) D. Guenzburger and E. M. Baggio Saitovitch, Phys. Rev. **24**, 2368 (1981).
[7] (a) D. G. Leopold and W. C. Lineberger, J. Chem. Phys. **85**, 51 (1986); (b) M. Moskovits and D. P. Dilella, *ibid.* **73**, 4917 (1980); (c) T. C. Devore, A. Ewing, H. F. Franzen, and V. Calder, Chem. Phys. Lett. **35**, 78 (1975); (d) S. Lin and A. Kant, J. Phys. Chem. **73**, 2450 (1969).
[8] S. K. Loh, L. Lian, D. A. Hales, and P. B. Armentrout, J. Phys. Chem. **92**, 4009 (1988).
[9] A. B. Anderson, J. Chem. Phys. **64**, 4046 (1976).
[10] H. Tatewaki, M. Tomonari, and T. Nakamura, J. Chem. Phys. **88**, 6419 (1988).
[11] E. A. Rohlfing, D. M. Cox, and A. Kaldor, J. Chem. Phys. **81**, 3846 (1981); D. M. Cox, R. L. Whetten, M. R. Zakin, D. J. Trevor, K. C. Reichmann, and A. Kaldor, Proc. Int. Laser Sci. Conf. 527 (1986).
[12] S. C. Richtsmeier, E. K. Parks, K. Liu, L. G. Pobo, and S. J. Riley, J. Chem. Phys. **82**, 5431 (1985).
[13] M. D. Morse, M. E. Geusic, J. R. Heath, and R. E. Smalley, J. Chem. Phys. **83**, 2293 (1985).
[14] M. R. Zakin, R. O. Brickman, D. M. Cox, and A. Kaldor, J. Chem. Phys. **88**, 6605 (1988).
[15] E. K. Parks, B. H. Weiller, P. S. Bechthold, W. F. Hoffman, G. C. Nie-

man, L G. Pobo, and S. J. Riley, J. Chem. Phys. **88**, 1622 (1988).
[16]Q. L. Zhang, S. C. O'Brien, J. R. Heath, Y. Liu, R. F. Curl, H. W. Kroto, and R. E. Smalley, J. Phys. Chem. **90**, 525 (1986).
[17]W. D. Knight, K. Clemenger, W. A. de Heer, W. A. Saunders, M. Y. Chou, and M. L. Cohen, Phys. Rev. Lett. **52**, 2141 (1984).
[18]J. A. Rutherford and D. A. Vroom, J. Chem. Phys. **65**, 4445 (1976); P. B. Armentrout, in *Structure/Reactivity and Thermochemistry of Ions*, edited by P. Ausloos and S. G. Lias (Reidel, Dordrecht, 1987), p. 97.
[19]K. Ervin, S. K. Loh, N. Aristov, and P. B. Armentrout, J. Phys. Chem. **87**, 3593 (1983).
[20]P. B. Armentrout, S. K. Loh, and K. Ervin, J. Am. Chem. Soc. **106**, 1161 (1984).
[21]See, for example, L. Hanley, S. A. Ruatta, and S. L. Anderson, J. Chem. Phys. **87**, 260 (1987); M. F. Jarrold, J. E. Bower, and J. S. Krauss, *ibid.* **86**, 3876 (1987).
[22]L. A. Bloomfield, R. R. Freeman, and W. L. Brown, Phys. Rev. Lett. **54**, 2246 (1985).
[23]L. Hanley and S. L. Anderson, J. Am. Chem. Soc. **91**, 5161 (1987).
[24]S. K. Loh, D. A. Hales, and P. B. Armentrout, Chem. Phys. Lett. **129**, 527 (1986).
[25]Disk source design is a modification of that contained in S. C. O'Brien, Y. Liu, Q. Zhang, J. R. Heath, F. K. Tittel, R. F. Curl, and R. E. Smalley, J. Chem. Phys. **84**, 4074 (1986).
[26]M. E. Geusic, M. D. Morse, S. C. O'Brien, and R. E. Smalley, Rev. Sci. Instrum. **56**, 2123 (1985).
[27]R. Campargue, J. Phys. Chem. **88**, 4466 (1984); J. P. Toennies and K. Winkelmann, J. Chem. Phys. **66**, 3965 (1977).
[28]Same concept as described in D. G. Leopold, K. K. Murray, A. E. Stevens Miller, and W. C. Lineberger, J. Chem. Phys. **83**, 4849 (1985).
[29]K. M. Ervin and P. B. Armentrout, J. Chem. Phys. **83**, 166 (1985).
[30]C.-S. Lu and H. E. Carr, Rev. Sci. Instrum. **33**, 823 (1962).
[31]Magnetic sector design considerations used are described by J. J. Livingood, *The Optics of Dipole Magnets* (Academic, New York, 1969), pp. 38–48.
[32]L. Kerwin, in *Mass Spectrometry*, edited by C. A. McDowell (McGraw–Hill, New York, 1963), p. 104.
[33]M. L. Vestal, C. R. Blakley, P. W. Ryan, and J. H. Futrell, Rev. Sci. Instrum. **47**, 15 (1976).
[34]K. M. Ervin, Ph.D. thesis, University of California, Berkeley, 1986.
[35]L. D. Landau and E. M. Lifshitz, in *Mechanics*, 3rd ed. (Oxford, New York, 1976), p. 93; H. G. Dehmelt, in *Advances in Atomic and Molecular Physics*, edited by D. R. Bates (Academic, New York, 1967), Vol. 3, p. 53.
[36]E. Teloy and D. Gerlich, Chem. Phys. **4**, 417 (1974); D. Gerlich, Diplomarbeit, University of Freiberg, Federal Republic of Germany, 1971.
[37]G. Mauclaire, R. Derai, S. Fenistein, and R. Marx, J. Chem. Phys. **70**, 4017 (1979).
[38]The ELFS lens is a dielectric lens supplied by the manufacturer to enhance mass resolution.
[39]N. R. Daly, Rev. Sci. Instrum. **31**, 264 (1959).
[40]R. W. Engstrom *Photomultiplier Handbook* (RCA, Lancaster, 1980).
[41]G. Gioumousis and D. P. Stevenson, J. Chem. Phys. **29**, 292 (1958).
[42]S. K. Loh, E. R. Fisher, L. Lian, R. H. Schultz, and P. B. Armentrout, J. Phys. Chem. (in press).
[43]N. Aristov and P. B. Armentrout, J. Phys. Chem. **90**, 5135 (1986).
[44]D. A. Hales, S. K. Loh, and P. B. Armentrout (work in progress).
[45]E. K. Parks, N. J. Hansen, and S. Wexler, J. Chem. Phys. **58**, 5489 (1973); E. K. Parks, A. Wagner, and S. Wexler, *ibid.* **58**, 5502 (1973); E. K. Parks, J. G. Kuhry, and S. Wexler, *ibid.* **67**, 3014 (1977).
[46]R. L. Hettich and B. S. Freiser, J. Am. Chem. Soic. **109**, 3537 (1987).
[47]P. J. Chantry, J. Chem. Phys. **55**, 2746 (1971).
[48]N. Aristov and P. B. Armentrout, J. Am. Chem. Soc. **108**, 1806 (1986); B. H. Boo and P. B. Armentrout, *ibid.* **109**, 3549 (1987); L. Sunderlin, N. Aristov, and P. B. Armentrout, J. Am. Chem. Soc. **109**, 78 (1987); J. L. Elkind and P. B. Armentrout, J. Phys. Chem. **91**, 2037 (1987).
[49]W. B. Maier II, J. Chem. Phys. **41**, 2174 (1964).
[50]R. D. Levine and R. B. Bernstein, Chem. Phys. Lett. **11**, 552 (1971).
[51]W. J. Chesnavich and M. T. Bowers, J. Phys. Chem. **83**, 900 (1979).
[52]P. J. Brucat, L.-S. Zheng, C. L. Pettiette, S. Yang, and R. E. Smalley, J. Chem. Phys. **84**, 3078 (1986).
[53]S. K. Cole and K. Liu, J. Chem. Phys. **89**, 780 (1988).
[54]M. F. Jarrold and J. E. Bower, J. Chem. Phys. **87**, 5728 (1987).
[55]C. Kittel, *Introduction to Solid State Physics* (Wiley, New York, 1976), pp. 136–9.
[56]Code written by W. L. Hase and D. L. Bunker; theory summarized by P. J. Robinson and K. A. Holbrook *Unimolecular Reactions* (Wiley–Interscience, New York, 1972).
[57]R. D. Levine and R. B. Bernstein, *Molecular Reaction Dynamics and Chemical Reactivity* (Oxford, New York, 1987), p. 103.
[58]T. A. Albright, J. K. Burdett, and M. H. Whangbo, *Orbital Interactions in Chemistry* (Wiley, New York, 1985).
[59]S. K. Loh, L. Lian, and P. B. Armentrout (work in progress).
[60]H. Purdum, P. A. Montano, G. K. Shenoy, and T. Morrison, Phys. Rev. B **25**, 4412 (1982).
[61]M. W. Chase, Jr., C. A. Davies, J. R. Downey, Jr., D. J. Frurip, R. A. McDonald, and A. N. Syverud, J. Phys. Chem. Ref. Data **14**, 1179 (1985).
[62]H. J. Freund and S. H. Bauer, J. Phys. Chem. **81**, 994 (1977).
[63]J. Sugar and C. Corliss, J. Phys. Chem. Ref. Data **14**, 407 (1985).
[64]N. Aristov and P. B. Armentrout, J. Phys. Chem. **91**, 5777 (1987).
[65]R. L. Hettich and B. S. Freiser, J. Am. Chem. Soc. **109**, 3537 (1987).
[66]N. W. Ashcroft and N. D. Mermin, *Solid State Physics* (Saunders College, Philadelphia, 1976), p. 461.
[67]R. D. Levine and R. B. Bernstein, *Molecular Reaction Dynamics and Chemical Reactivity* (Oxford, New York, 1987), p. 61.